

David Karl, Thomas Duminy, Pedro Lima, Franz Kamutzki, Albert Gili, Andrea Zocca, Jens Günster, Aleksander Gurlo

Clay in situ resource utilization with Mars global simulant slurries for additive manufacturing and traditional shaping of unfired green bodies

Open Access via institutional repository of Technische Universität Berlin

Document type

Journal article | Accepted version

(i. e. final author-created version that incorporates referee comments and is the version accepted for publication; also known as: Author's Accepted Manuscript (AAM), Final Draft, Postprint)

This version is available at


<https://doi.org/10.14279/depositonce-15716>

Citation details

Karl, D., Duminy, T., Lima, P., Kamutzki, F., Gili, A., Zocca, A., Günster, J., Gurlo, A. (2020). Clay in situ resource utilization with Mars global simulant slurries for additive manufacturing and traditional shaping of unfired green bodies. In *Acta Astronautica* (Vol. 174, pp. 241–253). Elsevier BV.

<https://doi.org/10.1016/j.actaastro.2020.04.064>.

Terms of use

 This work is licensed under a Creative Commons Attribution-NonCommercial- NoDerivatives 4.0 International license: <https://creativecommons.org/licenses/by-nc-nd/4.0/>

1

2

3 **Clay in situ resource utilization with Mars global simulant slurries for**
4 **additive manufacturing and traditional shaping of unfired green**
5 **bodies**

6

7

8 David Karl^{1*}, Thomas Duminy¹, Pedro Lima², Franz Kamutzki¹, Albert Gili¹, Andrea Zocca², Jens
9 Günster² and Aleksander Gurlo¹

10

11 **Affiliations:**

12 ¹ Fachgebiet Keramische Werkstoffe / Chair of Advanced Ceramic Materials, Institut für
13 Werkstoffwissenschaften und –technologien, Technische Universität Berlin, Germany

14 ² Bundesanstalt für Materialforschung und Prüfung (BAM), Berlin, Germany

15

16 *Correspondence to: david.karl@ceramics.tu-berlin.de

17 Telephone: +49(0)30 314 22368

18 Fax: +49(0)30 314 28534

1 **Abstract**

2 The wet processing of regolith simulant for clay in situ resource utilization (ISRU) on Mars is
3 presented. The two raw materials from the Mars global simulant family, one without clay (MGS-
4 1) and one with clay - sodium montmorillonite smectite - (MGS-1C) were milled and mixed to
5 produce a simulant with small particle size and reduced clay content (MGS-1C/8). All three
6 simulants and the pure clay raw material were extensively characterized using XRF,
7 synchrotron XRD, gas adsorption and gas pycnometry methods. In a straightforward processing
8 approach, MGS-1C/8 was mixed with water and different dispersant approaches were
9 investigated, all of which gave stable slurries. Particle size distribution, rheology, ion
10 concentration, pH and electrical conductivity of these slurries were characterized. The slurry
11 systems can easily be adapted to fit all typical ceramic shaping routes and here parts of varying
12 complexity from slip casting, throwing on a potter's wheel and additive manufacturing, including
13 material extrusion (robocasting) and binder jetting (powder bed 3D printing) were produced. The
14 unique properties of the sodium montmorillonite clay, which is readily accessible in conjunction
15 with magnesium sulfate on the Martian surface, acted as a natural nanosized binder and
16 produced high strength green bodies (unfired ceramic body) with compressive strength from 3.3
17 to 7.5 MPa. The most elaborate additive manufacturing technique layerwise slurry deposition
18 (LSD) produced water-resistant green bodies with a compressive strength of 30.8 ± 2.5 MPa by
19 employing a polymeric binder, which is similar or higher than the strength of standard concrete.
20 The unfired green bodies show sufficient strength to be used for remote habitat building on Mars
21 using additive manufacturing without humans being present.

22

1 **Keywords (6):** Mars smectite, clay ISRU, MGS-1 regolith simulant, 3D printing, slurry additive
2 manufacturing, wet processing, Martian habitat.

3

4 **Highlights:**

- 5 • Clay ISRU using wet processing with slurries can produce stable green bodies.
- 6 • During dispersion, magnesium salt interacts with clay, facilitating cation exchange.
- 7 • Five different shaping methods have been used to form complex green bodies.
- 8 • Green body comp. strength is 3.3-7.5 MPa without and 30.8 MPa with binder.
- 9 • Unfired green bodies show sufficient compressive strength for habitat building.

10

11

12

1. Introduction

In-detail exploration and subsequent colonization of Mars will only be feasible using in situ resource utilization (ISRU). This practice of on-site collection, processing, storing and use of local resources entails “hard ISRU” for infrastructure, such as landing pads, road, habitats and “soft ISRU” for human necessities such as food, consumables, i.e., everything inside a habitat [1]. In a previous publication, the authors discussed various material concepts for ISRU on the Moon and Mars [2], concluding that the production of ceramics from ground covering minerals/regolith is the most realistic early ISRU scenario for Mars. Previous studies for ceramic ISRU on Mars used the regolith simulant JSC-Mars-1A to introduce geopolymers [3], material extrusion with a phosphoric acid binder [4], sulfur concrete [5] and direct compression for blocks [6]. As none of the above approaches is used to a great extent on Earth, it is hard to assess their ISRU feasibility. In that respect, the authors have put forward the use of the oldest and most universal processing route towards ceramics - the wet processing of minerals into sintered ceramics [2]. Here, this wet processing route is further explored and the ISRU use of abundant clay and water resources on Mars for unfired and fired ceramics is proposed.

1.1 Clay ISRU on Mars

In their search for extraterrestrial life, researches have given out the dictum to “follow the water”, investigating water mineral interaction, which lead to a vast array of knowledge on different clay mineral resources on Mars [7]. The authors propose that this knowledge is of high value for ISRU efforts, as the shaping of clay minerals (one of the earliest human inventions originating before the Neolithic period) is a universal and versatile tool employed by all human civilizations. When humans have no access to what is called modern materials produced using vast amounts of energy, they resort to creating a built environment using locally available clay resources. This is illustrated by an estimation from 1994 of a third of the world’s population living in houses built of earth [8] and the United Nations Educational, Scientific and Cultural Organization (UNESCO)

1 lists as many as 150 structures built employing earthen architecture on their world heritage list
2 [9]. These can be found in mostly dry climates on all continents (except Australia) and include
3 Puebloan adobe houses, the mosques of Timbuktu, the Potala Palace of Lhasa, parts of the
4 Chinese great wall, frontiers of the Roman empire and also the ancient skyscrapers of Shibam
5 in Jemen, buildings made with blocks of clay earth that rise to 30 m and have 5 to 11 stories.
6 Recently, because of its passive environmental control and a significant reduction in embodied
7 energy, terrestrial earthen architecture has attracted attention. It has been estimated that sun-
8 baked unfired brick requires as little as 525.6 MJ/tonne energy while firing the same bricks to
9 around 900 to 1200 °C requires 4186.8 MJ/tonne - a difference of factor eight [10]. For Mars
10 ISRU, this illustrates a key strength of clay - on the one hand, the system can be used in the
11 unfired state for hard ISRU to build infrastructure, requiring minimal amounts of energy. On the
12 other hand, when properties such as high strength, water-resistance and gas tightness are
13 needed, the same material can be fired to produce sintered ceramics for soft ISRU.

14 **1.2 Choice of regolith simulants and wet processing**

15 The typical approach to conduct ISRU studies for Mars is the use of regolith simulants, with
16 JSC-Mars-1A having been used for most studies in the past. However, in the last decade data
17 produced by Curiosity's alpha particle X-ray spectrometer/diffractometer has dramatically
18 improved the understanding of Martian regolith and rocks, leading to the development of new
19 Martian simulants. A comprehensive overview of all Martian simulants was recently published
20 [11]. As of today, there are three distinct clay simulants which have taken Martian smectite
21 deposits into account: (i) P-MRS (Phyllosilicate Mars Regolith Simulant) with 45 wt.%
22 montmorillonite smectite and 5 wt.% of kaolinite [12], (ii) Y-Mars (Yellowknife-Mars) with 30.5
23 wt.% saponite smectite [13] and (iii) MGS-1C a variant of the Mars global simulant (MGS-1) with
24 40 wt.% sodium montmorillonite smectite [14,15]. All clay simulants face the challenge of low
25 terrestrial availability for nontronite and saponite (Fe/Mg smectites), that have been reported to

1 dominate on Mars [16]. While the saponite fraction for Y-Mars was painstakingly handpicked out
2 of vesicles in basalt, P-MRS and MGS-1C instead use the on Earth widely available
3 montmorillonite, an aluminum smectite that is also present on Mars [7]. For this work, the MGS-
4 1 simulant family was selected as it is modeled on crystalline and amorphous phases that are
5 similar to Gale crater regolith in mineralogical, spectral and physical properties [11], plus MGS-1
6 has excellent availability. Clay minerals are favorable for wet processing ISRU because of their
7 unique swelling behavior, which produces plastic bodies without the addition of plasticizers.
8 These bodies can be used in all wet shaping routes for ceramics, including remotely controlled
9 additive manufacturing techniques that could be used to build structures such as habitats
10 without humans being present on Mars.

11 In the proposed ISRU scenario, two kinds of raw minerals are envisaged that would be sourced
12 on the surface of Mars: (i) A clay soil from a phyllosilicate deposit and (ii) a soil used as a
13 temper, to reduce clay amount leading to improved slurry processability and mitigating
14 shrinkage plus cracking during drying (and sintering of the produced geometries). How essential
15 such tempering is for ceramic production becomes apparent when looking at artifacts from early
16 humans, such as 20,000 years old pots tempered with crushed quartzite or feldspar [17]. For
17 Mars, the importance of tempering sodium montmorillonite can also be inferred from desiccation
18 experiments and their extensive crack formation under Martian conditions [18].

19 The principal goal of this work was to develop a stable slurry system from MGS family simulants
20 and use such slurries in different wet processing approaches to shape green bodies for ISRU. In
21 the first part, the main material properties of MGS-1 family simulants and pure smectite
22 component used for MGS-1C are studied. These materials are adjusted and their dispersion in
23 water to generate stable slurries is explored. Obtained slurries and plastic bodies thereof are
24 processed via the traditional shaping methods slip casting, throwing on a potter's wheel plus the
25 additive manufacturing methods material extrusion (robocasting) and layerwise slurry deposition

1 (LSD), to produce high strength green bodies. An overview of the use of these different
2 technologies on Earth is given in Table 4. Furthermore, pressing of dry simulant powders is
3 used to produce reference green bodies. The mechanical properties, microstructure and
4 porosity of these green bodies are measured. A discussion of various proposed ISRU material
5 systems for ceramics on Mars finalizes the work.

6

1 **2. Materials and methods**

2 **2.1 Materials**

3 Two Martian regolith simulants (MGS-1 and MGS-1C) from the Mars global simulant family were
4 kindly supplied by Exolith Lab (CLASS/UCF, Orlando, USA). The MGS-1 open standard was
5 developed by Cannon *et al.* (2019) [14] based on Mars Science Laboratory (MSL) rover
6 Curiosity's X-ray diffraction results at Rocknest aeolian bedform, which is representative of
7 global basaltic soil at Gale crater on Mars [19]. The standard MGS-1 simulant, as well as a clay
8 modified version, denoted MGS-1C [15], was used. Exolith lab produces MGS-1C by mixing 40
9 wt.% smectite clay (sodium montmorillonite) into standard MGS-1 simulant. Kevin Cannon
10 kindly provided a small sample of the pure smectite for us to analyze. The amount of smectite in
11 MGS-1C is based on the hydrated clay reference case from a NASA Mars water in situ resource
12 utilization study [20]. Since Exolith lab does not provide provenance for the sodium
13 montmorillonite and as smectites vary considerably in their properties and behavior, the first aim
14 of this work was to establish the composition and basic properties of the smectite in MGS-1C
15 (see 3.1 results section, for evidence that all essential properties of the smectite are similar or
16 identical to Wyoming MX-80 bentonite). The final raw material for slurries was a mixture of
17 MGS-1 and MGS-1C, which is dubbed MGS-1C/8, as described in 2.2.1.

18

19 **2.2 Slurry preparation**

20 **2.2.1 Dry milling and tempering**

21 As delivered MGS-1 and MGS-1C simulants were milled separately using a steel milling vessel
22 in the vibratory disc mill TS250 (Siebtechnik GmbH, Germany). Each cycle consisted of milling
23 200 g powder in four two minute installments with two minute intermissions for cooling, to

1 prevent changes in powder properties due to heat. The milled powders were passed through a
2 250 μm sieve to break up (clay) agglomerates to guarantee uncomplicated dispersion. From
3 these powders, a new simulant composition with 5 wt.% montmorillonite (MGS-1C/8) was
4 produced by tempering MGS-1C with MGS-1. For this 12.5 wt.% MGS-1C (i.e., 1/8 - hence
5 MGS-1C/8) and 87.5 wt.% MGS-1 were dry mixed.

6 **2.2.2 Dispersion**

7 For the dispersion study, aqueous slurries with 60 wt.% MGS-1C/8 solid load were produced.
8 Three dispersion mediums were investigated: (i) Deionized water, (ii) deionized water with 0.1 to
9 0.5 wt% (on solid content) of the electrostatic inorganic polyanion dispersant Giessfix 162
10 (sodium disilicate) and (iii) deionized water with 0.26 to 8 wt.% of Dolapix PC67 (polycarboxylic
11 acid and sodium salt) an electrosteric sodium polyelectrolyte dispersant (both kindly supplied by
12 Zschimmer-Schwarz GmbH, Germany). For each slurry, MGS-1C/8 powder was carefully hand-
13 mixed into the respective dispersion medium and homogenized on a roll ball mill with 12 mm
14 ZrO_2 grinding balls for 10 minutes. For all shaping experiments, the original starting material
15 was an adjusted slurry system with 58 wt.% MGS-1C/8 and 0.5 wt.% PC67 specially modified to
16 meet requirements for layerwise slurry deposition (LSD). The mixing procedure was simplified
17 by subsequently pouring the powder into the liquid, which was being stirred vigorously from
18 overhead by impeller stirrer until all powder was wetted. The resulting slurry was aged for 24 h
19 and homogenized before use on a roller bank (without grinding balls) for 10 minutes.

20

21 **2.3 Shaping technologies**

22 **2.3.1 Slip casting**

23 For slip casting, a conical cup mold for porcelain made from casting plaster was generously
24 filled with MGS-1C/8 slurry and left to cast for 6 minutes to create thick-walled specimens. The

1 mold was emptied and rotated for 120 seconds to remove the excess slurry. After 24 hours, the
2 casts had detached and small casting failures were retouched with fresh slurry applied by a
3 brush. After the green body had dried, retouched areas were sanded using sandpaper with grit
4 size 1000.

5 **2.3.2 Shaping on potter's wheel and robocasting**

6 For throwing and robocasting, the MGS-1C/8 slurry water content was reduced to create plastic
7 bodies by pouring slurry onto filter paper that had been placed on a flat gypsum plate and left
8 until the solid/water percentage was 80 wt.% MGS-1C/8 solid load for throwing on the wheel
9 and 75 wt.% for robocasting. To throw a simple bowl, a circular polishing plate (Prätech Berlin
10 GmbH, Germany) was used as a potter's wheel at 25 to 50 rpm. For robocasting, an Ultimaker 2
11 go (Ultimaker B.V., Netherlands) was reequipped with a simple air-pressure controlled syringe-
12 style cartridge and a 0.84 mm diameter dispensing needle (both Vieweg GmbH, Germany) was
13 used to extrude the MGS ceramic paste (75 wt.% solids) at pressures ranging from 3 to 4 bar.

14 **2.3.3 Layerwise slurry deposition coupled with 3D printing**

15 Layerwise slurry deposition (LSD) is similar to binder jetting (also known as powder bed 3D
16 printing) but uses a slurry/slip as a feedstock instead of a powder. Very detailed descriptions
17 have been published on the custom-built LSD layer deposition setup for high-density powder
18 beds [21] and the use of this setup with inkjet printing [22,23]. In short, a doctor blade is used to
19 deposit 25-100 μm thick slurry layers on a base substrate and dried. Here, specific regions of
20 the single layers for cubic samples with $8 \times 6 \times 10 \text{ mm}^3$ (for compression tests) were infiltrated
21 using a proprietary resin binder ejected through an inkjet printhead, and the process was
22 repeated until a whole part was built. As motivational demonstrators of early civilizations,
23 Sumerian cuneiform tablet geometries were printed using STL files kindly provided by the Hub
24 at Colgate University. After the LSD process was finished, the whole powder bed block was
25 post-cured at 100°C for 12 hours and the printed green bodies were removed from high-density

1 powder beds by carefully washing with deionized water and left to dry in air for at least one
2 week.

3 **2.3.4 Dry pressing**

4 Dry pressing was used to produce square MGS-1C tiles with 6x6x1 cm³ and cylinders for green
5 compression tests with a diameter of 13 mm and a height of 27 mm. For this, stainless steel
6 dies were filled with 80 g for the tiles and 7.5 g for the cylinders of milled (but not pre-dried)
7 MGS-1C/8 powder (without dispersant) and pressed with an electric hydraulic press (Paul-Otto
8 Weber GmbH, Germany) at 70 MPa for 3 minutes.

9

10 **2.4 Characterization**

11 X-ray fluorescence (XRF) analysis of powders by melt tablet was performed with the
12 autosampler sequential wavelength X-ray spectrometer with Rh-anode PW 2400 (Panalytical,
13 Netherlands). Additionally, to determine SO₃ content in the samples (which could not be
14 measured using the specific version of the borate melt tablet method employed), pressed
15 powder tablets were analyzed. Iron content data given in Fe₂O_{3T} was recalculated to FeO_T by
16 division with the factor 1.1113. Synchrotron transmission X-ray powder diffraction (XRD) was
17 performed at beamline 12.2.2 of the Advanced light source (ALS) of the Lawrence Berkeley
18 National Laboratory (Berkeley, USA) with 25 keV radiation ($\lambda = 0.49594 \text{ \AA}$) in a setup described
19 previously [24,25]. Powder samples were placed in 700 μm quartz capillary sample holders and
20 measured in ambient air at room temperature. While the measurement for MGS-1 and MGS-
21 1C/8 were produced using an XRD 1621 image plate detector (Perkin Elmer, USA), MGS-1C
22 and pure smectite were measured using a MAR 345 (marXperts, Germany). For better
23 comparability with XRD data published by others (especially Karnland *et al.* [26]), XRD patterns
24 were calculated to Cu K α $\lambda = 1.5406 \text{ \AA}$. True powder particle density was determined using a

1 helium gas expansion multivolume pycnometer 1305 (Micromeritics Instrument Corp., USA) of
2 thoroughly dried powders (105°C for 72h under vacuum) using five repetitions and averaging
3 the results. Nitrogen adsorption with the Brunnauer, Emmet and Teller (BET) method was used
4 to determine the specific surface area (SSA) of dried powders employing a Quadrasorb station
5 (Quantachrome Instruments, USA) with two repetitions and averaging the results. Particle sizes
6 were obtained analyzing water dispersed powder/slurries in a wet cell of an LS 13 320
7 (Beckman Coulter, USA) laser diffraction particle size analyzer. Apparent viscosity and shear
8 stress of slurries were measured using a Physica MCR 301 rheometer (Anton Paar, Austria)
9 with 25 mm diameter parallel-plate geometry and 1 mm gap size. Slurry rheology and hysteresis
10 were measured at 25°C in rotation by increasing shear stress from 5 to 100 1/s and holding at
11 100 1/s to then decrease from 100 to 5 1/s again. A study on ion leaching/solubility behavior of
12 powders was devised by mixing selected powders in two percentages (at 0.99 wt.% and 58
13 wt.% solids) with deionized water and aging for 24 h. Half the volume of these slurries was
14 ultracentrifuged at 45000 rpm for 60 min using the Ultracentrifuge Optima L-90 K (Beckman
15 Coulter, USA) and the supernatant removed for analysis. pH and electrical conductivity were
16 measured on slurries and supernatants using a FiveEasy pH-meter (Mettler-Toledo Inc., USA)
17 and an inoLab Multi Level 1 (WTW GmbH, Germany) respectively. Ion concentrations of
18 systems without solids were measured by ICP-OES using an Ultima 2 (HORIBA SAS, France).
19 The apparent density of green parts was determined (with five samples for each shaping
20 technology) by measuring cube mass with a laboratory balance Genius ME215P (Sartorius,
21 Germany) and calculating the volume by measuring diameters with a Micromar micrometer
22 (Mahr GmbH, Germany). Micrographs of green parts were made using a scanning electron
23 microscopy (SEM) Gemini Leo 1530 (Carl Zeiss Microscopy GmbH, Germany) with acceleration
24 voltage ranging from 5 to 10 kV. The mechanical properties of green parts were evaluated using
25 compression tests. Samples with similar size and surface properties were shaped by
26 meticulously sanding green bodies from the four wet processing technologies using 1000 grit

1 sandpaper to cuboid shape with height/length/width of $16 \times 8 \times 4 \pm 1 \text{ mm}^3$. Sanding of dry pressed
2 samples was not feasible as they broke easily. Therefore, cylinder-shaped specimens directly
3 out of the press with a height of $27.5 \pm 0.3 \text{ mm}$ and a diameter of 13 mm were used for
4 compression tests. 5 specimens for each of the 5 shaping technologies were crushed using
5 plate on plate geometry on a RetroLine mechanical testing machine (Zwick/Roell, Germany)
6 with a loading rate of 70 kN/min.

7

8

9

1 **3. Results and discussion**

2 **3.1 Properties of raw materials and MGS-1C/8**

3 **3.1.1 Chemical composition**

4 XRF results of received MGS-1 and MGS-1C (Table 1), while generally similar, show some
5 variation from bulk chemistry given in Exolith datasheets, with small deviations for SiO₂, Al₂O₃,
6 FeO_T and more substantial discrepancies for CaO, MgO and Na₂O. On the one hand, the small
7 deviations are related to differences in data preparation of XRF results. While Cannon *et al.*
8 excluded loss on ignition, included SO₃ and calculated abundances to a sum of 100, the authors
9 included loss on ignition and excluded SO₃, which is why values from Cannon *et al.* tend to be
10 slightly higher. SO₃ values are reported from an analysis using the pressed tablet method, but
11 not taken into account when calculating major oxides (to correctly report results obtained using
12 the borate melt tablet method). On the other hand, it was suspected that deviations in
13 concentration could be related to unrepresentative sample taking, which is why element
14 chemistry for MGS-1C/8 (a tempered sample produced after the starting materials have been
15 thoroughly homogenized) was calculated by averaging values obtained from XRF analysis of
16 MGS-1 and MGS-1C. However, as the calculated and measured element chemistry for MGS-
17 1C/8 are an excellent match, the authors assumed that the more significant XRF deviations for
18 MGS-1 and MGS-1C stem from typical variations in bulk chemistry of the natural raw materials.

19

1

2 **Table 1:** Oxide constituents in wt.% for Rocknest soil, MGS-1 family simulants and clay references.

Com- pound	Regolith on Mars	MGS-1 Mars Global Simulant		MGS-1C Clay/Smectite MGS Simulant		Smectite Na- Montmorillonite		Smectite used for MGS-1C	MGS-1C/8 87.5% MGS-1 12.5 % MGS-1C	
	Rocknest soil ^a	Exolith Lab ^b	This paper ^c	Exolith Lab ^d	This paper ^c	SWy-2 CMS ^f	WyR1 MX80 ^g	This paper ^c	Calc. ^h	This paper ^c
SiO ₂	42.97	45.57	44.36	56.13	51.15	57.34	58.5	58.2	45.21	44.62
Al ₂ O ₃	9.37	9.43	12.71	16.89	13.98	17.89	19.1	18.28	12.87	12.92
FeO _T	19.18	16.85	11.90	8.24	10.86	3.36	3.42	3.15	11.77	11.25
MnO	0.42	0.1	0.1	0.04	0.05	0.01	n.a.	< 0.04	0.09	0.1
MgO	8.69	16.5	13.84	12.57	6.84	3.91	2.4	2.26	12.97	12.88
CaO	7.26	4.03	7.36	2.02	3.48	0.05	1.4	1.03	6.88	6.92
Na ₂ O	2.70	3.66	1.65	1.91	2.24	n.a.	2.1	2.2	1.72	1.73
K ₂ O	0.49	0.43	0.46	0.47	0.54	0.12	0.5	0.55	0.47	0.48
TiO ₂	1.19	0.3	0.39	0.21	0.28	0.11	0.2	0.14	0.38	0.35
P ₂ O ₅	0.95	0.37	0.11	0.35	0.09	0.02	0.0	0.05	0.11	0.11
Cr ₂ O ₃	0.49	0.12	0.13	0.02	0.04	n.a.	n.a.	-	0.12	0.12
SO ₃	5.47	2.63	(1.73) ⁱ	1.16	(1.05) ⁱ	n.a.	0.3	n.a.	(1.65)	(1.97) ⁱ
Cl	0.69	n.a.	n.a.	n.a.	n.a.	n.a.	n.a.	n.a.	n.a.	n.a.
LOI	n.a.	n.a.	5.53	n.a.	8.78	17.38	11.9	14.32	5.94	5.46
Total	99.87	99.99	98.54	100.01	98.33	100.19	99.82	100.18	98.53	96.94

3 ^a Curiosity rover APXS chem. compositions, bulk analyses of disturbed soil [27].4 ^b Developed by Exolith Lab, (MGS-1 datasheet Exolith Lab, August 2018 [28]).5 ^c Simulant analysed as delivered to TU Berlin by XRF with melt tablet method.6 ^d MGS-1C datasheet Exolith Lab, November 2018 [15].7 ^f Clay minerals society pure Wyoming Na-Montmorillonite [29].8 ^g Wyoming bentonite, 81-85 wt.% Na-Montmorillonite [26].9 ^h Calculated using TU Berlin MGS-1 and MGS-1C XRF analysis.10 ⁱ SO₃ determined by pressed powder tablet method, SO₃ not included in oxide calculation and total sum.

11

12

1 Furthermore, comparing Cannon *et al.* [14] with the recent Exolith lab datasheets for MGS-1
 2 [28], small changes in the amounts of ferrihydrite, hydrated silica, anhydrite and hematite should
 3 be noted (see Table 2), which is likely a result of finetuning the simulant's bulk chemistry (as
 4 proposed in Cannon *et al.* section 2.2.4). The chemical composition for the smectite component
 5 of MGS-1C corresponds to an analysis by Karnland *et al.* of MX-80, a Wyoming bentonite that
 6 consists of 81-85 wt.% sodium montmorillonite [26].

8 3.1.2 Phase composition

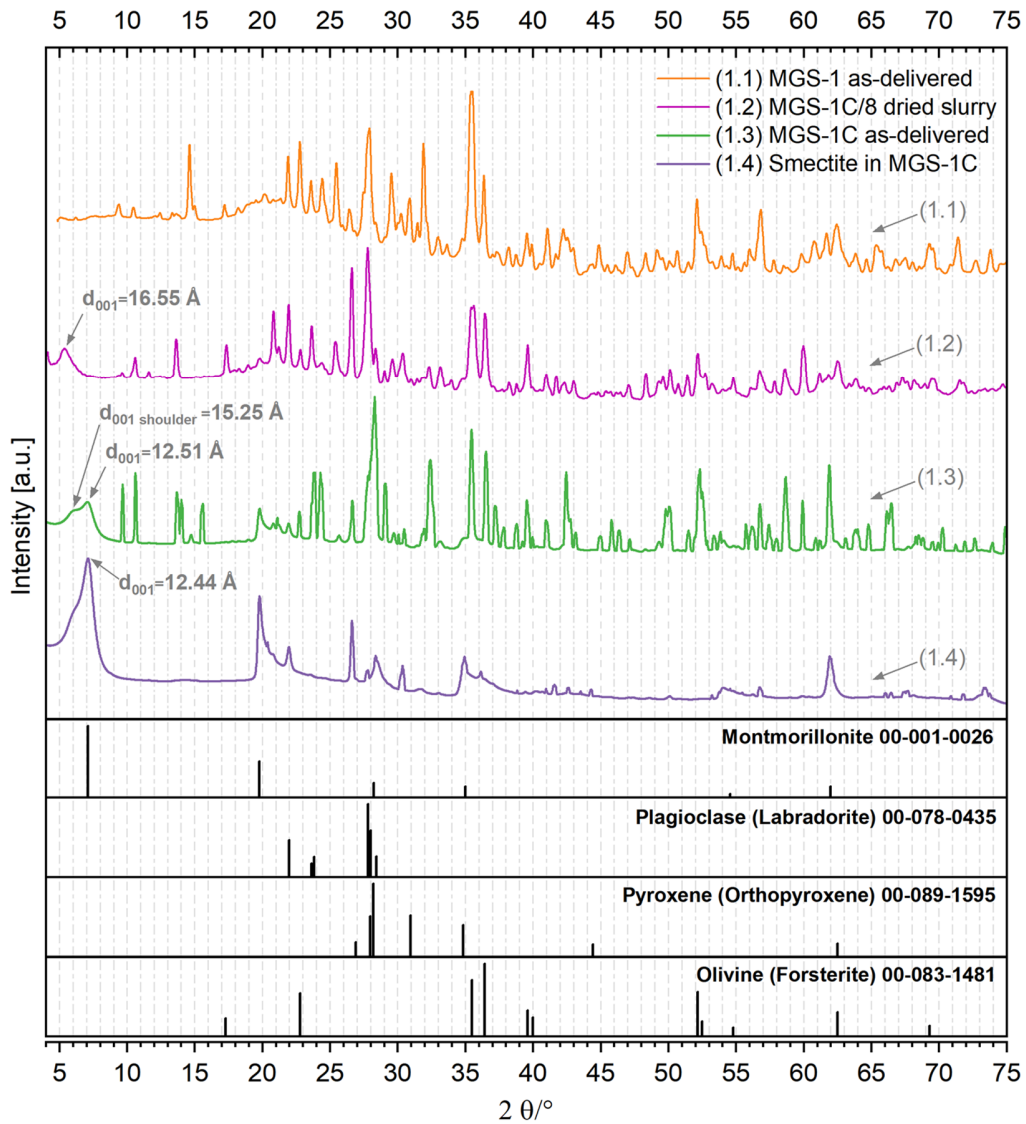
9 The XRD patterns in Fig. 1 for pure MGS-1 (1.1) show a high number of reflections as is to be
 10 expected from a material with a multitude of different crystalline components (Table 2).

11 **Table 2:** Phase composition (wt.%) of prototype MGS-1 and MGS-1 regolith simulants.

Reference	Plagioclase	Basaltic glass	Pyroxene	Olivine	Mg-sulfate	Ferrihydrite	Hydrated silica	Magnetite	Anhydrite	Fe-carbonate	Hematite
Cannon <i>et al.</i> [14]	27.1	22.9	20.3	13.7	4.0	1.7	5.0	1.9	0.9	1.4	1.1
Exolith datasheet [28]	27.1	22.9	20.3	13.7	4.0	3.5	3.0	1.9	1.7	1.4	0.5

12
 13 Comparing XRD patterns of the three samples that contain MGS-1 (1.1 to 1.3) the most obvious
 14 differences are in the region from 8° to 18° degree. After 20°, a comparison is hindered by the
 15 complexity (even though most of the prominent reflections are present in all three patterns). Due
 16 to this complexity, only the three major crystalline silicate components from the MGS-1 recipe
 17 are referenced in Fig. 1. The largest recipe constituent is plagioclase with 27.1 wt.%, which
 18 Cannon *et al.* in turn comprised of a not specified combination of anorthosite, plagioclase and
 19 labradorite. A reference file for labradorite fits major reflections between 20° and 30° two theta

1 in the MGS-1 sample (1.1 to 1.3) patterns. The second biggest crystalline component in the
2 recipe is pyroxene with 20.3 wt.% made of what Cannon *et al.* describe as bronzite-variety
3 pyroxene. Evaluating their XRF data for this pyroxene (see their Table 1 in Supplementary
4 Information [14]), the authors propose it can be better described as a hypersthene composition
5 with an approximate Fe/Mg ratio of 1:1 $\sim(\text{Fe}_{0.5}\text{Mg}_{0.5})_2\text{Si}_2\text{O}_6$. The orthopyroxene doublet at 28°
6 two theta is especially pronounced for (1.3) but is shifted to the labradorite doublet slightly below
7 28° for (1.1) and (1.3). Furthermore, the pyroxene peak at 31° is only pronounced in (1.1) and
8 absent in (1.3). According to the recipe of Cannon *et al.* the third main crystalline component
9 with 13.7 wt.% is forsteritic olivine. All three patterns (1.1) to (1.3) show the forsterite reflections.
10



1
 2 **Fig. 1:** Synchrotron XRD patterns (calculated to Cu $K\alpha$ $\lambda=1.5406$ Å) of pure MGS-1 (1.1), MGS-1 with 5
 3 wt.% (1.2) and 40 wt.% (1.3) smectite as well as pure smectite (1.4) plus bar charts of main reflections
 4 from powder diffraction files (PDF) for montmorillonite, labradorite, orthopyroxene and forsterite.

5
 6 For pure smectite (1.4), the synchrotron XRD diffractogram is a good match for diffractograms
 7 from Karnland *et al.* (2006) of MX-80 bentonite (their Figure 3-7) [26]. Using Rietveld
 8 quantitative XRD analysis Karnland *et al.* give calculated mean results for three XRD

1 measurements of this WyR1 sample with sodium montmorillonite (83.5 wt.%), feldspars (2.9
2 wt.%), quartz (2.8 wt.%), muscovite (2.8 wt.%), gypsum (0.9 wt.%), cristobalite (0.4 wt.%) and
3 calcite (0.2 wt.%) [26]. While dry sodium montmorillonite has a d_{001} spacing of ~ 9.7 Å [30,31],
4 here $d_{001} = 12.44$ Å was found. This fits the measurement in ambient air and is in good
5 agreement with Kraehenbuehl *et al.* (1987) who reported for MX-80 with 5 wt.% water that each
6 interlayer cation absorbs 6 H₂O molecules leading to swelling with $d_{001} = 12.3$ Å [30] and similar
7 to the $d_{001} = 12.65$ Å from Monte Carlo simulations at 6 H₂O per O₂₀(OH)₄ [31]. MGS-1C (1.3)
8 showed a similar d_{001} of 12.51 Å and a pronounced shoulder at 15.25 Å, (a smaller shoulder at
9 this angle is also visible in (1.4)). This shoulder stems from mixed interlayer cations and mixed
10 hydration states: Kraehenbuehl *et al.* have reported a similar 15.1 Å for MX-80 with ≤ 10 wt.%
11 water absorption [30] and Karnland *et al.* have reported a Na⁺/Ca²⁺ exchangeable cation ratio in
12 MX-80 bentonite of 75 % charge from Na⁺ and 17 % charge from Ca²⁺ [26]. As it is known, that
13 calcium montmorillonite only forms two-layer hydrates [31] the shoulder should stem from Ca²⁺
14 interlayer cations that are hydrated with 12 H₂O per O₂₀(OH)₄. The noteworthy shift to a basal
15 spacing of 16.55 Å for dried MGS-1C/8 (1.2) is indicative of a cation exchange from sodium to
16 magnesium montmorillonite during MGS-1C/8 dispersion due to the high concentration of Mg²⁺
17 ions from the 4 wt.% magnesium sulfate component in MGS-1C. Monte Carlo simulations for
18 montmorillonite show that minerals with divalent cations expand at lower water content
19 compared to systems with monovalent cations plus divalent systems do not form single-layer
20 hydrates [31]. The divalent Mg ions have larger hydration energy and such systems can
21 accommodate more water, which is apparent in TG measurements of sodium montmorillonite
22 with a weight loss of 95 % at 200 °C, compared to the same system with cation exchanged
23 magnesium with a weight loss of 90 % [32]. Comparing the $d_{001} = 16.55$ Å with simulations from
24 Teich-McGoldrick *et al.* (their Figure 2 at 298 K), it is expected that the dried slurry system with
25 cation exchanged magnesium montmorillonite (1.3) has absorbed 11 H₂O per O₂₀(OH)₄ during
26 the XRD measurement in ambient air [28].

1

2 **3.1.3 True density**

3 The 2.740 g/cm³ true density for pure smectite (Table 3) was a good match with the 2.750 -
4 2.755 g/cm³ found in literature for MX-80 sodium montmorillonite [33,34]. MGS-1 particle density
5 has not been reported before. The 3.041 g/cm³ found puts MGS-1 density in the region of non-
6 weathered pristine Martian basalt that has a grain density > 3 g/cm³ [14]. Measured densities for
7 mixtures of MGS-1 with smectite (MGS-1C and MGS-1C/8) are in agreement with mixture
8 calculations using obtained values for the single components.

9

10 **Table 3:** Density and specific surface area for raw materials ordered with decreasing clay content.

Compound	True density ρ_{true} (g/cm³)	BET specific surface area (m²/g)
Smectite	2.740 ± 0.006	24.6 ± 1.7
MGS-1C	2.951 ± 0.011	16.31 ± 0.06
MGS-1C/8	2.996 ± 0.009	7.11 ± 0.17
MGS-1	3.041 ± 0.002	8.35 ± 0.18

11

12 **3.1.4 Specific surface area**

13 While montmorillonite has a total theoretical SSA in the range of 750 m²/g [33], nitrogen
14 absorption can only be used to measure the external SSA of the material because nitrogen
15 atoms cannot enter the montmorillonite's interlayer surfaces in the dry/non-swollen state.

16 Conforming to this is a dependence of measured SSA on the drying procedure. After drying for
17 24 h at 105 °C under vacuum, SSA for smectite was 26.32 m²/g. This area decreased to 22.87
18 m²/g when the same material was measured again after drying 96 h at the same conditions,
19 which is indicative of the smectite's extreme affinity to water, as 24 h drying did not remove all

1 the interlayer water from the material. A similar dependence of SSA on drying procedure for
2 MX-80 has been reported by Karnland *et al.* comparing milling, oven-drying and freeze-drying
3 [33]. For oven-drying, they report an SSA of 23.8 m²/g, which is in good accordance with the
4 22.87 m²/g measured here, but slightly different from the 30.29±0.22 found by others [35]. While
5 SSA for MGS-1 and MGS-1C are in the expected range, MGS-1C/8 has a slightly smaller SSA
6 compared with MGS-1, which is surprising as it contains 5 wt.% smectite. Calculating SSA using
7 obtained values for smectite and MGS-1 gives a value of 9.17 m²/g. It is assumed that this
8 stems from the dry milling of MGS-1C/8, which might have led to an agglomeration process of
9 the finest particle fraction that typically has a high effect on SSA of non-porous materials.

10

11 **3.2 Slurry development**

12 **3.2.1 Optimization of particle size distribution**

13 As described in 2.2.1 two raw materials were mixed to create the new simulant MGS-1C/8 with
14 custom-fit clay content and particle size distribution (PSD) for ideal dispersion and processing.
15 For this, the PSD (Fig. 2) of as-delivered, coarse MGS-1 (2.1) and MGS-1C (2.2) was tailored
16 by dry milling and subsequent tempering to create MGS-1C/8 (2.4), a powder with 5 wt.% clay
17 content and a PSD below 100 µm.

18 While being well aware that wet milling is considered favorable for particle dispersion, as newly
19 created fractured surfaces are always chemically active [36], dry milling with a rotary mill was
20 chosen as it is fast and initial wet milling trials with typical roller bank equipment revealed that a
21 fraction of large particles in MGS simulants could not easily be wet milled below 100 µm.

22

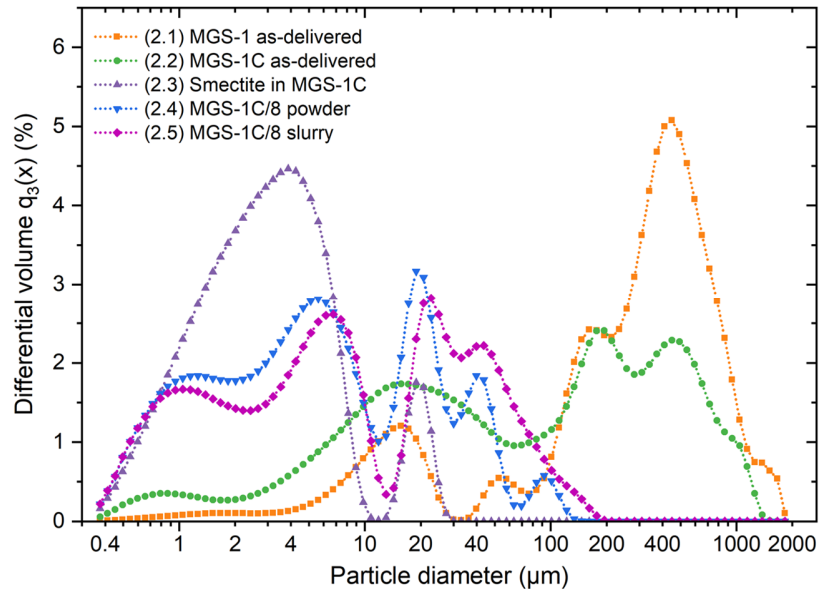


Fig. 2: Particle size distribution of raw, milled powders and MGS-1C/8 slurry.

1

2

3

4 The swelling effect of MGS-1C/8 in water can be seen at the shift towards larger PSD from

5 MGS-1C/8 powder (2.4) to MGS-1C/8 slurry (2.5) that had been aged in water. However, there

6 is no significant difference for PSD of both (2.4 and 2.5) below 1 μm , which is surprising as

7 dispersed MX-80 consists of plates with an irregular shape and a bimodal PSD, with one

8 population 400 nm long, 250 nm wide and 1 nm thick and the other 65 nm long and 35 nm wide

9 and 1 nm thick [37]. That no change $< 1 \mu\text{m}$ was observed could be related to resolution

10 limitations due to high obscuration levels from the small smectite particles and/or general

11 limitations for particle detection using Fraunhofer diffraction theory on particles with small sizes.

12 Resolution limitations would also explain why PSD for pure smectite (2.3) is slightly below (2.4)

13 and (2.5), even though the smectite is not mixed with milled MGS-1 powder, which is expected

14 to have a low number of particles $> 2 \mu\text{m}$ (as a result of the used milling method). The authors

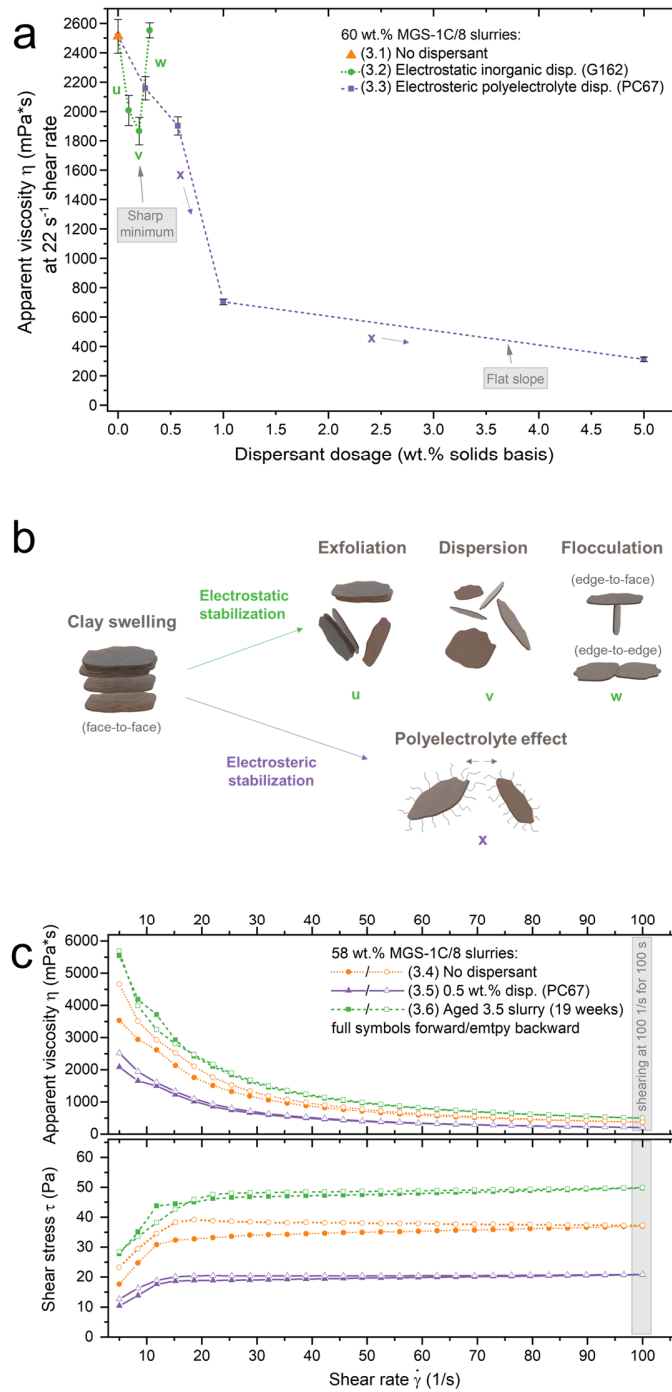
15 hypothesized that the 5 wt.% sodium montmorillonite acts as a nanophase binder and the single

16 smectite sheets build agglomerates with bigger MGS-1 particles, as can be seen from the shift

17 starting from 10 μm .

1 **3.2.2 Rheology of MGS-based slurries**

2 While initial trials with pure MGS-1C (40 wt.% smectite) in water produced strong pastes (that
3 could not be used for shaping), tempering to 5 wt.% smectite (MGS-1C/8) gave well-dispersed
4 slurries with all three dispersant approaches (no dispersant; electrostatic; electrosteric) when
5 applied in the suggested doses of 0.1 to 0.5 % of the solids content (Fig. 3a) producing
6 viscosities in a similar range. Dispersion with the ionic sodium disilicate (3.2) produced a sharp
7 viscosity minimum as the particles have their maximum mobility. Adding more electrostatic
8 dispersant leads to ionic solvation immobilizing liquid and increased viscosity (Fig. 3b, -
9 subimage w). From an ISRU standpoint, the use of a simple sodium disilicate would be
10 preferable to dispersants with polymeric components, but the sharp minimum reduces
11 processing flexibility significantly. Contrary to this, the polyelectrolyte electrosteric dispersant
12 (3.3) (polymer chains of the polycarboxylate component attach themselves to clay particles and
13 effect electrosteric repulsion, see Fig. 3b - subimage x) showed an extraordinarily broad
14 processing window with a flat minimum as even dosages of 5 to 8 wt. % (data not shown) did
15 not increase the apparent viscosity. For shaping experiments, the electrosteric dispersant PC67
16 was chosen, even though higher weight fractions are needed for such dispersants compared
17 with electrostatic inorganic dispersants. Essential considerations for this decision were: (i) the
18 risk of overdosage is significantly reduced, (ii) the viscosity minimum is lower and (iii) pure
19 sodium dispersants tend to be problematic for slipcasting as sodium cations migrate into the
20 gypsum mold and slowly disintegrate it by solution weakening [36].



1

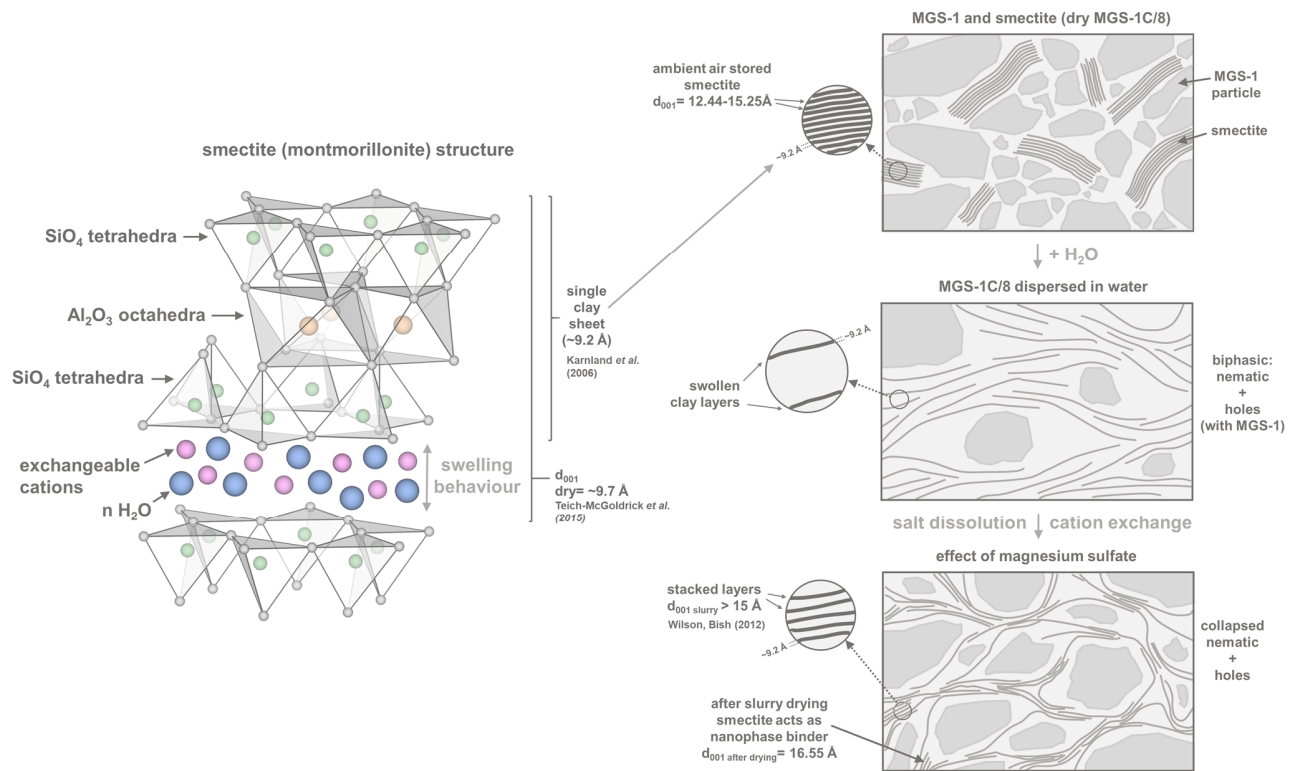
2 **Fig. 3:** (a) Multipoint rheograms of MGS-1C/8 slurries with 60 wt.% solids loading at a low shear rate,

3 (b) artist's impression of electrostatic and electrosteric stabilization and (c) flow and viscosity curves of

4 MGS-1C/8 slurries with 58 wt.% solids loading optimized for LSD.

1

2 For LSD, the final MGS-1C/8 with PC67, dispersant proportion was fixed to 0.5 wt.% and the
3 slurries solids content was reduced from 60 to 58 wt.% to counteract a tendency to hold air
4 bubbles (leading to occasional air pores in LSD layers), further reducing viscosity and abolishing
5 the issue. In general, apparent viscosities for LSD slurries should be slightly higher compared to
6 slip casting slurries. A reference porcelain slurry for slip casting had the apparent viscosity of
7 265 mPas at 22 s^{-1} shear rate [2] compared to 894 ± 36 mPas at the same rate for LSD MGS-
8 1C/8 slurry. A comparison of the rheology for this slurry (after 24 h and aged for 19 weeks) with
9 a no dispersant slurry (Fig. 3c) suggests that LSD would also be possible for slurries with no
10 dispersant as all three systems have a similar rheology profile in the range of LSD processability
11 [22]. This similarity is likely to be the result of the 4.0 wt.% magnesium sulfate component of
12 MGS-1, which Cannon *et al.* added in the form of epsomite ($\text{MgSO}_4 \cdot 7\text{H}_2\text{O}$) and which dissolves
13 altogether producing Mg^{2+} aquacations and sulfate anions when MGS-1 is mixed with water due
14 to epsomite's high solubility of 113 g/100 mL at 20°C , increasing ionic strength of the solution. It
15 has been shown that sodium montmorillonite/water dispersions with low ionic strength show a
16 behavior that is diphasic (see Fig. 4 middle texture) with a nematic phase (particles aligned in
17 loose parallel lines) and holes [38]. Upon the increase of ionic strength, which is especially
18 pronounced here as the multivalent Mg^{2+} ions contribute strongly to ionic strength, the nematic
19 phase collapses to form denser sediments (Fig. 4 bottom texture). This stems from the
20 compression of the diffusive layer around clay particles due to high ionic strength leading to a
21 reduction of distance over which the electrostatic repulsive forces are effective and a tendency
22 for clay particles to flocculate [39]. Hence, the governing mechanism for MGS-1C/8 slurry
23 rheology with and without dispersant is proposed to be related to the high ionic strength due to
24 epsomite dissolution and it is assumed that this flocculation mechanism leads to the stabilization
25 of larger non-clay MGS-1 in the suspension (Fig. 4 bottom texture).



1
 2 **Fig. 4:** Smectite structure and artists' impression of different textures of MGS-1C dispersion with the
 3 effect of magnesium sulfate (edited from [38]). Basal spacings (d_{001}) for smectite are from XRD results
 4 (Fig. 1) and marked literature references.

5
 6 From an ISRU standpoint, it is noteworthy that the magnesium sulfate finds wide application as
 7 a flocculant in ceramics, as it thickens and gels slurries which are then stable for long periods
 8 [40], even facilitating thixotropic (shear thinning) glaze formulations without clay, that can be
 9 homogeneously applied on dense-sintered ceramics.

10 For the MGS-1/8 slurry without dispersant, it is expected that the Mg^{2+} and Ca^{2+} dominance
 11 (Fig. 5.6) and absence of electrosteric dispersant (PC67) shift the particles further towards
 12 flocculation which is related to the hysteresis loop found in the rheogramm for this slurry (3.4).

13 While hysteresis with decreased resistance caused by shearing is often reported for clay

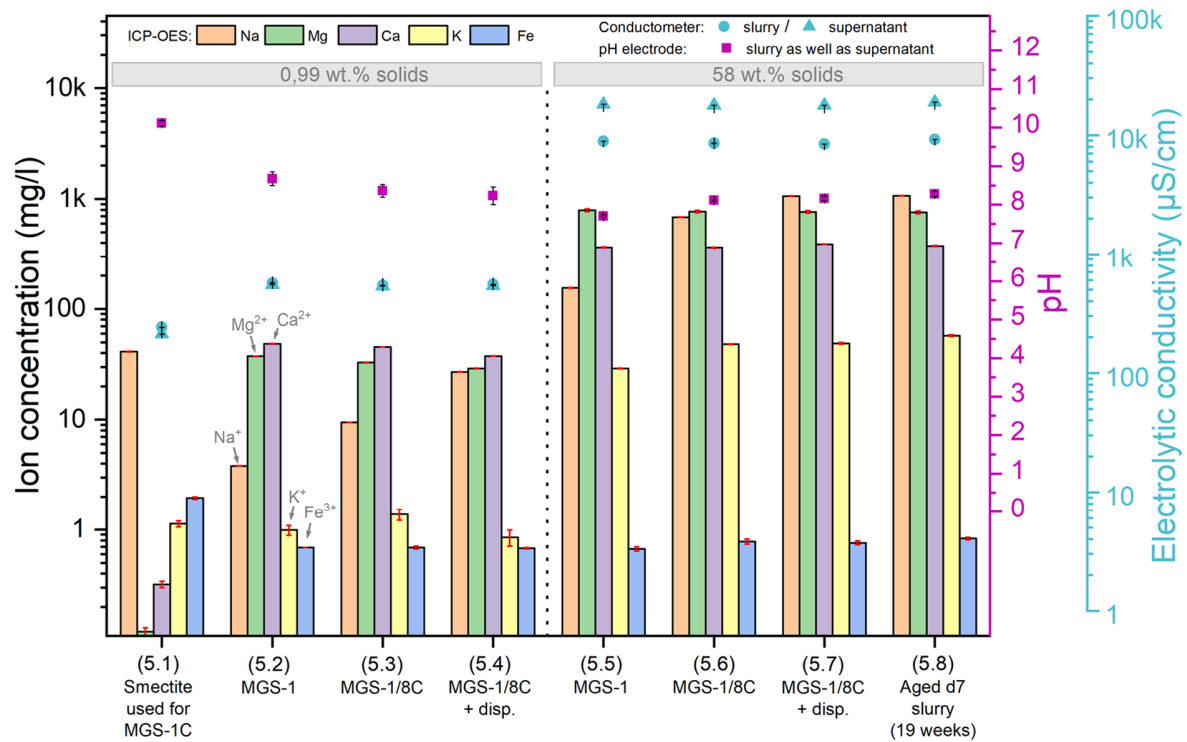
1 rheology [41,42], here the rare case of slightly increased resistance (rheopectic behavior) after
2 shearing the slurry for 100s at 100 1/s is observed. A comparable behavior was reported by
3 Jeong *et al.* for a similar sodium montmorillonite sample (their Figure 12) [43]. This dependence
4 of rheology on shear history was not as pronounced for the two slurries with dispersant (3.5
5 and (3.6), which was all the more reason to choose the 0.5 wt.% dispersant proportion for LSD
6 and further shaping experiments. Looking at the systems processing stability over time, aging
7 was observed. An increase in apparent viscosity after 19 weeks (3.6), but no significant leaching
8 seemed to have taken place, as ion concentrations stayed in a similar range (Fig. 5.8) and
9 principal rheological behavior was similar. This implies that slurries can be continuously used
10 over long periods by adjusting processing parameters. In conclusion, the authors proposed that
11 the interaction of sodium montmorillonite and magnesium sulfate is enough to stabilize Martian
12 slurries for shaping over long periods and no dispersant would be needed for clay ISRU. What
13 is more, not only has it been suggested that magnesium sulfate is common on the Martian
14 surface, but that magnesium sulfate is typically found in association with smectites and that both
15 resources are easily accessible [44].

16 In addition, the authors assume that all major smectite species found on Mars (montmorillonite,
17 nontronite and saponite) could be used interchangeably (with small adaptations) to produce
18 slurries with comparable properties: All three smectites have similar cation and anion exchange
19 capacity [45]. While montmorillonite and saponite show similar morphology and size (with thin
20 platelets and films) [46], nontronite platelets have generally similar size but exhibit a lathed
21 shape [47]. Dispersion behavior has been reported to be comparable, with 6 wt.% Wyoming
22 montmorillonite and California saponite slurries (autoclaved at different temperatures) showing
23 similar viscosities [46]. Furthermore, dispersions of 0.5 wt.% Montmorillonite and Nontronite
24 also had matching viscosities [48].

25

1 3.2.3 Ion concentration, pH and electrical conductivity

2 Several previous studies have established the dependence of montmorillonite swelling and
3 rheology of montmorillonite suspensions on the availability of exchangeable cations (Mg^{2+} , Ca^{2+} ,
4 Na^+ , etc.). While systems with Mg^{2+} and Ca^{2+} tend to flocculate and have the highest hydration
5 enthalpies promoting swelling [31], Na^+ cations tend to bring the system towards deflocculation
6 [40]. Sodium cations in the MGS-1/C8 slurry system originate from the smectite (sodium
7 montmorillonite) and the dispersant (PC67). As epsomite levels stay constant, Mg^{2+} ion
8 concentration (Fig. 5) was found to be on a similar level from (5.2) to (5.4) and (5.5) to (5.7)
9 respectively, but there is a shift in the Mg^{2+}/Na^+ ratio with a significant increase of Na^+ ions to
10 1063 mg/L as compared to 785 mg/L Mg^{2+} ions constituting a Na^+ majority for the MGS-1/C8
11 with dispersant (5.7). However, XRD evidence (1.4) for this dried slurry (5.7) indicates a cation
12 exchange to Mg^{2+} ions after dispersion and drying, which can be explained by a significantly
13 higher absorption selectivity for Mg^{2+} on montmorillonite particles compared to Na^+ . Rytwo *et al.*
14 reported that montmorillonite particles in 2.4 wt.% aqueous suspension of Wyoming bentonite
15 with 544 mg/L Na^+ ions and 423 mg/L Mg^{2+} ions (which is a similar Mg^{2+}/Na^+ ratio to (5.7)),
16 absorbed 0.06 ± 0.02 mol/kg Na^+ and 0.78 ± 0.05 mol/kg Mg^{2+} (their table 3) [49]. This high
17 absorption selectivity for Mg^{2+} is especially noteworthy as the starting Na^+ concentrations in the
18 solution were higher compared to Mg^{2+} .



1
 2 **Fig. 5:** Ion concentration of supernatants from slurries with 0.9 and 58 wt.% solid content and pH as well
 3 as electric conductivity of these slurries and their supernatants.

4
 5 During slurry development, no apparent correlation between viscosity and pH could be
 6 established as solutions of magnesium sulfate have pH ~ 7, also adding PC67 dispersant (5.4
 7 and 5.7) did barely influence pH. A slight pH dependence was observed for (5.1) that had a high
 8 Na⁺ ratio with an increased pH and for (5.5) that had a low Na⁺ ratio, which produced a slightly
 9 lower pH. The lack of Mg²⁺ ions (5.1) sharply reduced electrical conductivity, while the addition
 10 of dispersant had almost no effect. However, it is noteworthy that electrical conductivity for
 11 solutions without and with (58 wt.%) particles (5.5 to 5.8) could be predicted from models
 12 previously reported [50], as non-conducting solids did not transport charges.

13

1 **3.3 Shaping**

2 **3.3.1 Dry pressing**

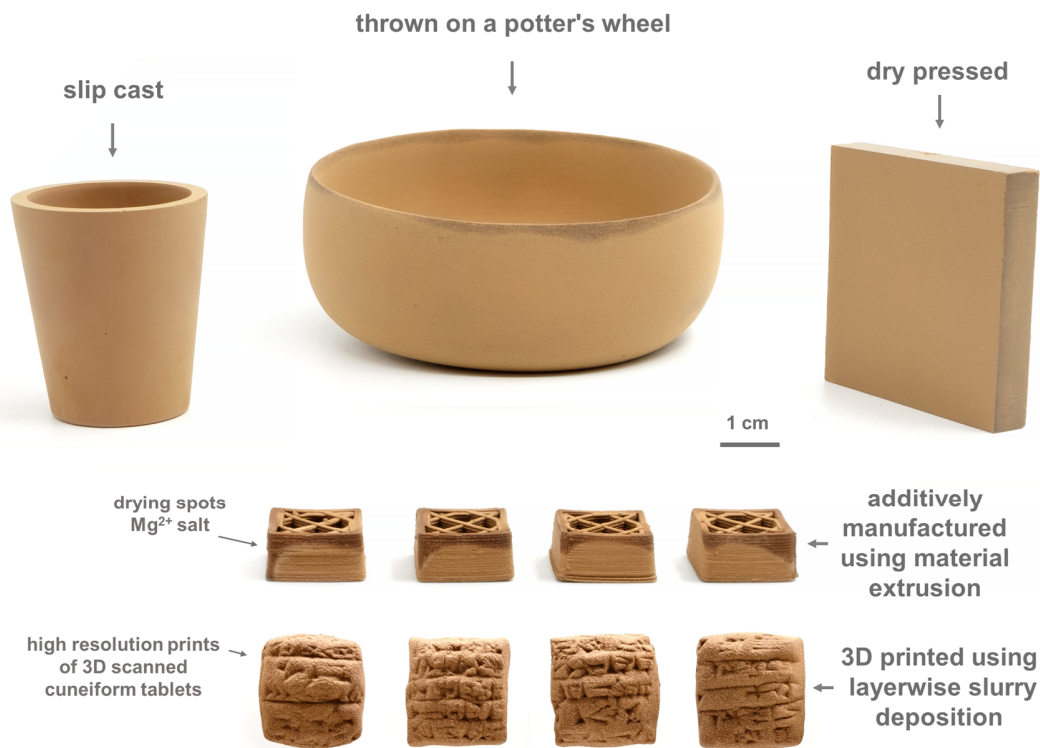
3 Tiles of the MGS-1C/8 powder with sufficient integrity for careful demolding could be dry
4 pressed without adding any binders. However, samples had to be stored in a desiccator, as tiles
5 left in ambient air absorbed water, which led to local swelling in pressing direction (starting from
6 the corners).

7

8 **3.3.2 Slip casting**

9 As the slurry was optimized to work for LSD, the most complex shaping technology, it had a
10 thixotropic behavior and after filling the slip casting molds, gelling was observed, which made
11 removing excess slurry from the cast challenging and produced parts with larger thickness.
12 Furthermore, demolding was found to be challenging, as shrinkage in the initial wet stage was
13 very minimal due to slow water removal, which is typical for sodium montmorillonite. Using a
14 clod test, Tadza found Wyoming smectite (MX-80) to shrink roughly seven times longer and
15 significantly more than a kaolin sample [51]. Without slurry modification, only parts with low
16 complexity such as rings and a simple cup (see Fig. 6) could be demolded without breaking. For
17 the future, these issues can be overcome by reducing slurry thixotropy, setting up a special
18 drying regime, using other dispersants with better mold release properties (e.g., polyacrylate
19 family [36]) and by coating mold walls with demolding agents (e.g., 5 % sodium alginate in water
20 [52]).

21



1
 2 **Fig. 6:** Shaping of green bodies with the versatile MGS-1C/8 slurry system using classic pottery (potter's
 3 wheel), slip casting, material extrusion (robocasting/direct ink writing), 3D printing (layerwise slurry
 4 deposition with binder jetting) and as a reference dry pressing.

5
 6 **3.3.3 Hand building/throwing on a potter's wheel**

7 Reducing slurry water amount on plaster produced pastes that were either very plastic and
 8 sticky at 75 wt.% solids (used for robocasting) or medium plastic and non-sticky at 80 wt.%
 9 solids (used for throwing). Here, already finished LSD slurry was repurposed by reducing water
 10 content with a method commonly used in potter studios. The final water content can be
 11 controlled by changing the time the slurry is on the plaster plate (when the added
 12 volume/thickness plus spread area on to the plate is fixed). Even though the plaster plate
 13 method is straightforward for specialized feedstock production, the authors propose to simplify

1 the whole workflow for the production of pastes by directly mixing powders and corresponding
2 water amount, followed by aging. While the 80 wt.% paste could in principle be shaped on a
3 pottery's wheel, a sudden change from medium to high plasticity was encountered when adding
4 water onto the paste (by wet hands), leading to body instability. When no water was used,
5 plasticity was low and thin walls tended to break. Even though the humidity was controlled
6 during drying, large shrinkage and (for thin-walled structures) stress release by crack formation
7 was observed.

8 Nonetheless, modeling thick-walled structures worked well and the authors conclude that
9 pressing the paste into molds to produce high-density bricks would be feasible.

10

11 **3.3.4 Material extrusion using robocasting**

12 Extrusion of 75 wt.% paste worked well with nozzle diameters down to 0.84 mm, while reducing
13 diameter further led to clogging (with the simple syringe set-up and a maximum pressure of 6
14 bar). The system was set to slight over-extrusion to overcome air bubbles left in the syringe (no
15 degassing was necessary), which fused layers well. Minor warping after drying on plywood
16 plates was observed, which could be mitigated by controlled drying and careful selection of the
17 printing substrate. A peculiar phenomenon in connection to the slow montmorillonite drying and
18 the use of magnesium sulfate was observed. The sections of parts (especially from robocasting
19 and slip casting) to dry last had a darker surface (see robocast parts in Fig. 6), which is
20 concluded to stem from efflorescence. As a result of the high magnesium sulfate solvability, the
21 salt migrated to regions that dried last, which were the corners of robocast parts and the inside
22 of slip cast parts. Furthermore, differences in chemistry for the darker regions are to be
23 expected, as white and yellow scumming (color dependant on temperature) was observed after
24 sintering the samples (results not shown).

1 Finally, the MGS-1C/8 system showed excellent process flexibility for robocasting without
2 further adjustments, and the possibility of a wide application range for material extrusion AM on
3 Mars is envisioned, especially in the construction of large structures such as buildings.

4 5 **3.3.5 Layer-wise slurry deposition with 3D printing**

6 Initial trials for layer deposition with slurries from pure MGS-1C (40 wt.% smectite) showed
7 intensive crack formation due to the high shrinkage of the montmorillonite component. This can
8 be explained by biaxial stresses in the layer from constrained shrinkage as each new layer
9 firmly adheres to the already dried preceding one. The magnitude of the biaxial stresses
10 depends on the specific material shrinkage stress versus layer strength. Typically, clay
11 materials are exceptionally well suited for the LSD process as their plasticity can accommodate
12 such biaxial stresses [23] and once slurries were tempered to 5 wt.% smectite (MGS-1C/8) the
13 issue of crack formation was overcome. Also, with preliminary MGS-1C/8 slurries that had 60
14 wt.% solids load, a tendency to hold air bubbles was noticed, which lead to occasional air pores
15 in the powder bed. Subsequently, the system was thinned to 58 wt.% solids load and the
16 resulting slurry (which was used for all further LSD experiments) showed a very stable
17 deposition behavior and produced layers without cracks and air pores. However, compared to
18 other ceramics slurries, MGS-1C/8 layers dried slowly, which is indicative of montmorillonite's
19 exceptional water retention behavior.

20 In this work, the layerwise slurry deposition was combined with binder jetting to define the cross-
21 sections of the parts in every layer and to provide these with sufficient strength. The
22 combination of these technologies is the so-called LSD-print process. The printed binder is a
23 proprietary resin that is entirely cross-linked after post-treatment at 100°C for several hours. At
24 this stage, the parts achieve a strength sufficient to immerse the powder bed in water and wash
25 away the surrounding powder. After washing and drying, the parts show a considerable strength

1 due to the high powder packing and the organic binding phase, which typically consists of <15
2 vol.% of the bodies depending on the parameters used. Here, TG experiments (data not shown)
3 suggest that after drying the resin component amounted to as little as < 5 wt.% of the LSD
4 green parts. Of all the techniques presented in this work, LSD is the most advanced and
5 sophisticated. Due to the labor-intensive washing away of the surrounding powder bed, the
6 technique is not well suited for early ISRU scenarios. However, LSD has its strength in the
7 production of high-resolution sintered ceramics with low failure probability. Especially for silicate
8 ceramics, the use of inorganic binders fitting the LSD-print approach can be foreseen. Binders
9 like sodium silicate could be synthesized from Martian soil minerals, possibly leading to a full
10 ISRU approach. Furthermore, the use of such ISRU binders to increase green strength and
11 water resistance is a very promising concept, that can be combined with the other wet
12 processing techniques introduced here.

13

14 **3.3.6. Comparing ISRU feasibility of different shaping routes**

15 A comparison of dry pressing and all four wet processing routes for green body ISRU on Mars
16 can be found in Table 4. While, LSD with 3DP and slip casting are deemed more appropriate for
17 classic sintered ceramics (as they produce bodies of small to medium size with great detail but
18 require more labor and equipment), extrusion or press molding of single bricks, as well as
19 robocasting (and combinations of all three), have great potential for infrastructure production on
20 Mars.

21

22

1
2

Table 4: Examples for the use of different shaping technologies on Earth and assessment of requirements for green body ISRU on Mars.

Shaping technology ^a	Use on Earth ^b	Mass of equipment required ^c	Other materials needed ^{c,d}	Total energy required for process ^{c,e}
Dry pressing	Simple shaped ceramic parts: Tiles, fireclay bricks, structural clay, porcelain products	high	none	high
Slip casting	Complex shaped part (with fine details): Sanitary ware, tableware, and porcelain.	low	ISRU gypsum for molds	low
Hand deformation of clay bodies	Throwing of pottery, press molding of mud bricks/adobe bricks.	low	none	low
Material extrusion	Forming of parts with one cross-section (and unlimited length): Clay brick, tile, vitrified clay pipe (sewer pipes), porcelain insulators	medium	none	medium
Material extrusion (robocasting)	Vases, artistic objects, clay walls/houses.	low	none	medium
Tape casting/doctor blade processing	Production of thin ceramic plates: Thin porcelain tiles or layerwise slurry deposition (high-density small objects with good resolution)	high	binder system for LSD ^f	very high

3

^a Main categories were used.

4

^b Commonly used on Earth to shape which clay-based green bodies.

5

^c Assessed for Mars ISRU on a five-point scale: none, low, medium, high, very high.

6

^d Additional ISRU resources needed (assuming MGS-1C/8 without dispersant is used).

7

^e Including energy needed for the preparation of feedstock (sorting, milling, etc.).

8

^f Inorganic ISRU binders could be developed or polymeric binder ISRU produced (needed ~ 5 wt.%).

9

10

11

12

13

3.4 Density, porosity and mechanical properties of fabricated parts

3.4.1 Density, porosity and microstructure of green bodies

Dry pressing produced green bodies with the highest density with 2.05 g/cm³ and lowest porosity with 31.8 % (Fig. 7).

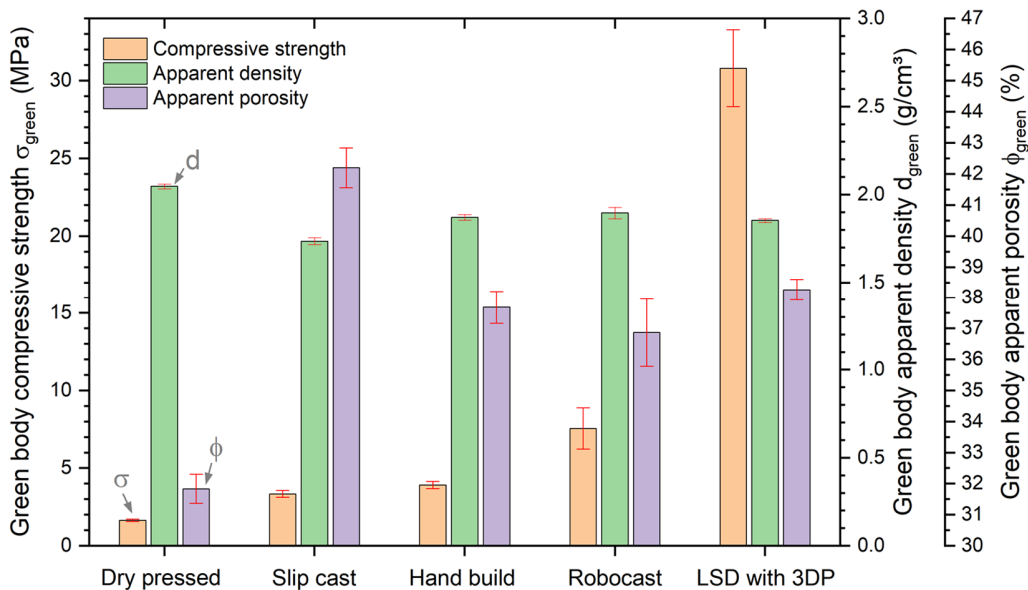
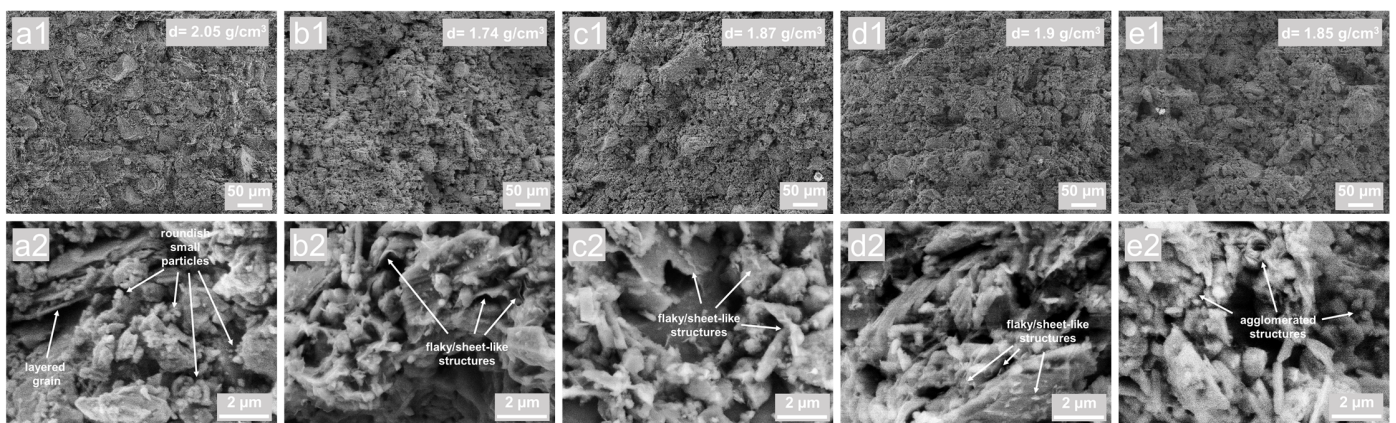


Fig. 7: Compressive strength (σ), density (d) and porosity (Φ , calculated from pycnometer density) of green bodies.

Micrographs of the green body rupture surface for this sample Fig. 8 (a1) show a relatively dense microstructure with large grains embedded in a surrounding matrix. The two shaping processes employing a paste produced the highest densities for wet processed samples, led by robocasting with 1.90 g/cm³ followed by hand building with 1.87 g/cm³ and their micrographs are quite similar (c1) and (d1). Finally, the processes using a slurry, slip casting and LSD showed the slightly lower densities with 1.74 g/cm³ and 1.85 g/cm³. This agrees with the higher number of pores (especially for slip casting) in micrographs (b1) and (e1). It is assumed that lower

1 density and higher porosity (42.2 %) for slip casting are related to the thixotropic slurry behavior,
 2 which is associated with lower particle mobility during casting, inhibiting self-
 3 compaction/ordering of particles from capillary forces during cake formation. The same can be
 4 applied to LSD density, as the process of cake formation is essentially the same and the higher
 5 density for LSD green bodies compared to slip cast ones is expected to stem from binder
 6 infiltration during printing. High-resolution micrographs give indications of the processing
 7 methods, for example, in the image of the dry pressed sample (a2), a grain with a layered
 8 structure can be observed in the background top left. This grain can be assumed to either be a
 9 large clay particle or a mineral grain broken from compression during dry pressing and such
 10 structures are not observed in the wet processed samples. While small particles in the dry
 11 pressed sample (a2) have a round morphology, all wet processed samples without binder (b2)
 12 to (d2), have a somewhat flaky or thin sheet-like structure for their small particles. It is
 13 reasonable to assume these are smectite sheets surrounding larger MGS-1 particles, as
 14 proposed in the bottom texture in Fig. 4. For LSD (e2), such small particle sheet structures are
 15 not prominent and larger particles dominate that are agglomerated, which is proposed to be a
 16 result of the resin binder used for LSD.



17 **Fig. 8:** SEM micrographs of green body fracture surfaces for dry pressed (a), slip cast (b), hand build (c),
 18 robocast (d) and LSD (e) samples.

1

2 **3.4.2 Mechanical properties**

3 Following observations from sample grinding, dry pressed samples showed the lowest
4 compressive strength by far with 1.64 ± 0.08 MPa. All wet processed samples, while having a
5 lower apparent density, showed at least twice the compressive strength and more than fourfold
6 this value for Robocast samples (7.55 ± 1.33 MPa), which had the highest compressive strength
7 for samples without a binder. Comparing robocasting to hand building, the almost twofold
8 increase of strength plus higher standard deviation for robocasting is assumed to be related to
9 the anisotropy inherent in the extrusion process, a topic that will be investigated in future work.

10 The results clearly indicate that wet processing (even when producing lower green density) is
11 superior to dry processing for green body strength of MGS-1C/8. This can be attributed to two
12 principal phenomena that occur for wet processing during drying of slurries. On the one hand,
13 there is a self-ordering of particles due to the mobility of particles in the dispersion leading to
14 particle interlocking. On the other hand, it is well known that the drying of suspensions will
15 produce agglomerates. Even though agglomeration is a universal phenomenon during drying,
16 the phenomenon is not fully understood. It has been proposed that agglomeration stems from
17 the pulling together of discrete particles, as a result of capillary forces due to air-water interfaces
18 during drying [53]. Another proposed mechanism is related to the dissolution of matter from the
19 dispersed powders into the liquid phase [54]. During drying, the dissolved matter precipitates at
20 particle contact points to form interparticle necks, leading to solid bridges characteristic of hard
21 agglomerates.

22 In this context, the essential reason why dry pressed green strength is markedly different to wet
23 processed for MGS-1C/8 is related to clay swelling and ion dissolution-precipitation. First, wet
24 processing leads to the separation of the montmorillonite clusters into single sheets (see Fig.
25 **3b**). The amount of nanosized particles produces a high specific surface area and leads to a

1 dramatic increase in the number of points-of-contact. Second, it is assumed that the ions
2 dissolved from montmorillonite and magnesium sulfate during wet processing (see Fig. 5) plus
3 slurry dispersant is precipitated at the contact point producing solid bridges during drying and
4 thus increasing green body strength. The two mechanisms seem to be specially marked for
5 montmorillonite (compared to other clays such as kaolinite), in that swollen montmorillonite with
6 its very small particles acts as a natural nanophase binder, which is why bentonite is used by
7 potters as an additive to increase green strength of their wares for better handling.

8 The MGS-1C/8 green strength of slip cast (3.34 ± 0.22 MPa) and thrown (3.91 ± 0.23 MPa)
9 samples compare well to the size-dependent compressive green strength of 2.58 to 3.48 MPa
10 Wong *et al.* found for small spherical aggregates of bauxitic clay formed by spray drying [55].
11 Similarly, robocast green strength (7.55 ± 1.33 MPa) is in line with the 4.5 to 6.4 MPa Heath *et al.*
12 found for dry unfired extruded bricks, which they proved is sufficient structural capacity to
13 construct a two-story domestic building [8]. Thus, evaluating MGS-1C/8's usefulness in
14 construction, all wet processing methods produced green bodies with an air-dry strength
15 exceeding the specified minimum compressive strength of 1.5 MPa for load-bearing walls of
16 autoclaved aerated concrete (a foam concrete masonry material) [56] which is widely used for
17 buildings. What is more, LSD printed sample with a polymeric binder (that would have to be
18 shipped or produced locally from the atmosphere) did not dissolve during immersion in water
19 and showed values for green body strength of 30.8 ± 2.47 MPa. This is in the region of general-
20 purpose concrete, which typically has >20 MPa after 28 days and even surpasses a much-cited
21 study by Cesaretti *et al.* on binder jetting of lunar regolith using the D-shape technology with a
22 magnesium salt binder producing compressive strength of 20.35 MPa [57]. In general, the
23 concept of using binders on clay green bodies is promising as the organic binder could be
24 switched to ISRU produced inorganic binders such as geopolymers and lime stabilizers that
25 have been reported as binders for unfired clay masonry [10,58].

3.4.3 Comparing various ISRU material concepts

The clay material system presented here makes use of readily available minerals that can be utilized and processed into a final product with the lowest amount of energy required for all so far proposed IRSU materials the authors are aware of and shows decent compressive strength. Comparing with previous studies, all other materials and processing approaches have higher energy or shipping/sourcing requirements (see Fig. 9), while some report better compressive strength.

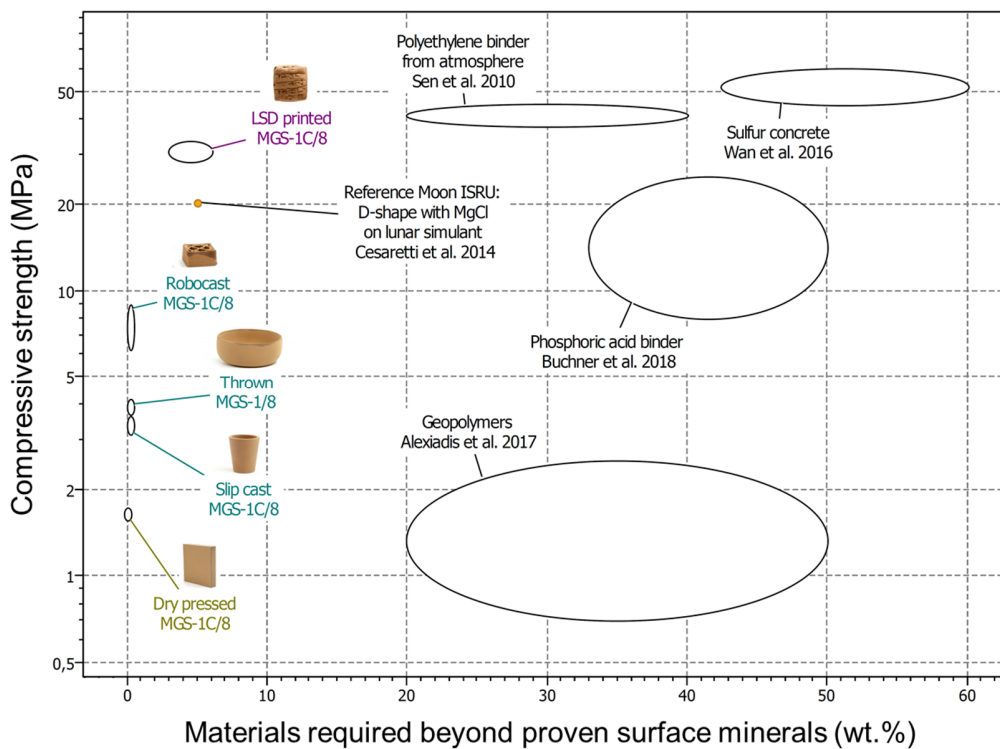


Fig. 9: Compressive strength of green bodies over additional materials required (aside from regolith and clay minerals) for Mars ISRU material systems and a reference study for Moon ISRU [57].

Geopolymer bricks produced with significant amounts of K_2SiO_3 and $NaOH$ (both not readily available on Mars) had a relatively low compressive strength of 0.7 to 2.5 MPa [3]. Use of a concentrated phosphoric acid liquid (at least 33 wt.% would have to be shipped) gave decent

1 parts with a compressive strength of around 20 MPa [4]. Composites with 20 wt.% ISRU
2 polyethylene binder, which would have to be synthesized from the atmosphere, had a
3 compressive strength of 41.1 MPa [59]. The fusion of regolith with 50 wt.% molten sulfur
4 (unclear local raw material availability, heating of materials) produced parts with a compressive
5 strength of over 50 MPa [5]. In another category is the dry pressing of small blocks employing
6 high pressures (10 times the values used for dry pressing in this work), which gave parts with a
7 flexural strength of 10 to 50 MPa [6]. Due to the high energy usage and similar mechanical
8 properties, it seems appropriate to instead compare these with slip cast ceramics from JSC-
9 Mars-1A with a Weibull flexural strength of 15 to 51 MPa [2].

10 Contrary to this, the MGS-1C/8 system presented here, would not require shipping of any
11 chemicals, as the processing equipment and slurry can be adjusted to work well without the 0.5
12 wt.% dispersant, currently added. It is proposed that extrusion or press molding of single bricks,
13 as well as robocasting (and combinations of all three), are highly promising construction
14 technologies for hard IRSU, especially in the dry environment on Mars, where humidity will not
15 impede green body strength. What is more, green bodies produced here can be sintered into
16 ceramics with excellent mechanical properties (with bending strength between terracotta and
17 porcelain), which the authors will report on in a subsequent publication.

18

1 **4. Conclusions**

2 The Mars global simulant raw materials and pure clay component used for slurries were
3 extensively characterized and it was proposed that the smectite component is equivalent to the
4 Wyoming bentonite MX-80. Inspired by the use of clay in human history, the development of a
5 highly versatile clay slurry system, solely using resources easily accessible on the Martian
6 surface, is presented. The system exploits the cation exchange behavior of smectite clay with
7 magnesium sulfate and both resources are commonly found in association on Mars. The
8 developed production route is straightforward and can theoretically be custom fit to work with all
9 wet ceramic shaping technologies, four of which were presented here. As the produced green
10 bodies can be used in the unfired state for modern clay construction or in the fired state as
11 Martian pottery/ceramics a multitude of applications in hard and soft ISRU is foreseen. In the
12 future, it is planned to improve the green body's stability using lime and geopolymer binders and
13 to investigate the structures under Martian atmospheric and temperature conditions.
14 Additionally, it is planned to enhance compressive strength by employing fillers such as coarse
15 regolith and basalt fibers. The most likely early ISRU on Mars is a robocasting scenario to build
16 habitats, using robotic arms with big enough extrusion nozzles to produce full-scale structures.
17 NASA's Mars 2020 rover mission is planned to return samples from the surface of Mars for the
18 first time. Its landing site will be Jezero crater and delta, where different smectite-bearing rock
19 units have been detected [60]. The authors expect the in-detail investigation of Martian clays
20 from this sample return mission to increase confidence in simulant mineral compositing and
21 generate widespread interest for clay ISRU.

22

1 **Acknowledgments**

2 David Karl would like to thank the Evonik Stiftung for their financial support. We thank Mathias
3 Czasny (TU Berlin) for retrofitting an Ultimaker printer with the robocasting setup. Furthermore,
4 we thank Petra Marsiske for XRF, Christina Eichenauer for BET and Harald Link for ICP (all TU
5 Berlin). We thank Exolith lab for supplying simulants and their service to the ISRU community.
6 This research used resources of the Advanced Light Source, which is a DOE Office of Science
7 User Facility under contract no. DE-AC02-05CH11231.

8

9 **Data availability**

10 The raw data required to reproduce these findings will be made available on request.

11

1 **References**

- 2 [1] K.M. Cannon, D.T. Britt, Feeding One Million People on Mars, *New Space* 7 (2019) 245–
3 254. <https://doi.org/10.1089/space.2019.0018>.
- 4 [2] D. Karl, F. Kamutzki, A. Zocca, O. Goerke, J. Guenster, A. Gurlo, Towards the colonization
5 of Mars by in-situ resource utilization: Slip cast ceramics from Martian soil simulant, *PloS*
6 *one* 13 (2018) e0204025. <https://doi.org/10.1371/journal.pone.0204025>.
- 7 [3] A. Alexiadis, F. Alberini, M.E. Meyer, Geopolymers from lunar and Martian soil simulants,
8 *Advances in Space Research* 59 (2017) 490–495. <https://doi.org/10.1016/j.asr.2016.10.003>.
- 9 [4] C. Buchner, R.H. Pawelke, T. Schlauf, A. Reissner, A. Makaya, A new planetary structure
10 fabrication process using phosphoric acid, *Acta Astronautica* 143 (2018) 272–284.
11 <https://doi.org/10.1016/j.actaastro.2017.11.045>.
- 12 [5] L. Wan, R. Wendner, G. Cusatis, A novel material for in situ construction on Mars:
13 Experiments and numerical simulations, *Construction and Building Materials* 120 (2016)
14 222–231. <https://doi.org/10.1016/j.conbuildmat.2016.05.046>.
- 15 [6] B.J. Chow, T. Chen, Y. Zhong, Y. Qiao, Direct Formation of Structural Components Using a
16 Martian Soil Simulant, *Scientific reports* 7 (2017) 317. [https://doi.org/10.1038/s41598-017-](https://doi.org/10.1038/s41598-017-01157-w)
17 [01157-w](https://doi.org/10.1038/s41598-017-01157-w).
- 18 [7] B.L. Ehlmann, C.S. Edwards, Mineralogy of the Martian Surface, *Annu. Rev. Earth Planet.*
19 *Sci.* 42 (2014) 291–315. <https://doi.org/10.1146/annurev-earth-060313-055024>.
- 20 [8] A. Heath, D. Maskell, P. Walker, M. Lawrence, C. Fourie, Modern earth masonry: structural
21 properties and structural design. *The Structural Engineer* 90 (2012) 38-44,
22 <http://www.istructe.org/webtest/files/60/6093d338-aa24-4ff8-8de5-99bc757940f8.pdf>
23 (accessed 20 December 2019).

- 1 [9] D. Gandreau, L. Delbo, Inventory of earthen architecture. 2012. UNESCO, Paris,
2 <https://unesdoc.unesco.org/ark:/48223/pf0000217020> (accessed 20 December 19).
- 3 [10] J.E. Oti, J.M. Kinuthia, Stabilised unfired clay bricks for environmental and sustainable
4 use, *Applied Clay Science* 58 (2012) 52–59. <https://doi.org/10.1016/j.clay.2012.01.011>.
- 5 [11] N.K. Ramkissoon, V.K. Pearson, S.P. Schwenzer, C. Schröder, T. Kirnbauer, D. Wood,
6 R.G.W. Seidel, M.A. Miller, K. Olsson-Francis, New simulants for martian regolith:
7 Controlling iron variability, *Planetary and Space Science* (2019) 104722.
8 <https://doi.org/10.1016/j.pss.2019.104722>.
- 9 [12] U. Böttger, J.-P. de Vera, J. Fritz, I. Weber, H.-W. Hübers, D. Schulze-Makuch,
10 Optimizing the detection of carotene in cyanobacteria in a martian regolith analogue with a
11 Raman spectrometer for the ExoMars mission, *Planetary and Space Science* 60 (2012)
12 356–362. <https://doi.org/10.1016/j.pss.2011.10.017>.
- 13 [13] A.H. Stevens, E. Steer, A. McDonald, E.S. Amador, C.S. Cockell, Y-Mars: An
14 Astrobiological Analogue of Martian Mudstone, *Earth and Space Science* 5 (2018) 163–174.
15 <https://doi.org/10.1002/2017EA000318>.
- 16 [14] K.M. Cannon, D.T. Britt, T.M. Smith, R.F. Fritsche, D. Batchelder, Mars global simulant
17 MGS-1: A Rocknest-based open standard for basaltic martian regolith simulants, *Icarus* 317
18 (2019) 470–478. <https://doi.org/10.1016/j.icarus.2018.08.019>.
- 19 [15] CLASS Exolith Lab, Datsheet for MGS-1C Clay ISRU: (November 2018). Cannon, Kevin
20 M., Conroy, Mike, Britt, Daniel T. University of Central Florida, USA,
21 https://sciences.ucf.edu/class/simulant_mgs1c (accessed 18 April 2020).
- 22 [16] J.F. Mustard, S.L. Murchie, S.M. Pelkey, B.L. Ehlmann, R.E. Milliken, J.A. Grant, J.-P.
23 Bibring, F. Poulet, J. Bishop et al., Hydrated silicate minerals on Mars observed by the Mars

- 1 Reconnaissance Orbiter CRISM instrument, *Nature* 454 (2008) 305.
2 <https://doi.org/10.1038/nature07097>.
- 3 [17] X. Wu, C. Zhang, P. Goldberg, D. Cohen, Y. Pan, T. Arpin, O. Bar-Yosef, Early pottery
4 at 20,000 years ago in Xianrendong Cave, China, *Science* (New York, N.Y.) 336 (2012)
5 1696–1700. <https://doi.org/10.1126/science.1218643>.
- 6 [18] M.R. El-Maarry, A. Pommerol, N. Thomas, Desiccation of phyllosilicate-bearing samples
7 as analog for desiccation cracks on Mars: Experimental setup and initial results, *Planetary
8 and Space Science* 111 (2015) 134–143. <https://doi.org/10.1016/j.pss.2015.03.021>.
- 9 [19] D.L. Bish, D.F. Blake, D.T. Vaniman, S.J. Chipera, R.V. Morris, D.W. Ming, A.H.
10 Treiman, P. Sarrazin, S.M. Morrison et al., X-ray diffraction results from Mars Science
11 Laboratory: Mineralogy of Rocknest at Gale crater, *Science* (New York, N.Y.) 341 (2013)
12 1238932. <https://doi.org/10.1126/science.1238932>.
- 13 [20] A. Abbud-Madrid, D. Beaty, D. Boucher, B. Bussey, R. Davis, L. Gertsch et al., Mars
14 water in-situ resource utilization (ISRU) planning (M-WIP) study: 90 p, posted (April 2016).
15 California Institute of Technology,
16 https://mepag.jpl.nasa.gov/reports/Mars_Water_ISRU_Study.pdf (accessed 20 April 2020).
- 17 [21] T. Muehler, C. Gomes, M.E. Ascheri, D. Nicolaidis, J.G. Heinrich, J. Guenster, Slurry-
18 Based Powder Beds for the Selective Laser Sintering of Silicate Ceramics: *Journal of
19 ceramics science and technology, Journal of Ceramic Science and Technology* 6 (2015)
20 113–117. <https://doi.org/10.4416/JCST2015-0007>.
- 21 [22] A. Zocca, P. Lima, J. Günster, LSD-based 3D printing of alumina ceramics, *Journal of
22 Ceramic Science and Technology* 8 (2017) 141–147. [https://doi.org/10.4416/JCST2016-
00103](https://doi.org/10.4416/JCST2016-
23 00103).

- 1 [23] P. Lima, A. Zocca, W. Acchar, J. Günster, 3D printing of porcelain by layerwise slurry
2 deposition, *Journal of the European Ceramic Society* 38 (2018) 3395–3400.
3 <https://doi.org/10.1016/j.jeurceramsoc.2018.03.014>.
- 4 [24] A. Doran, L. Schlicker, C.M. Beavers, S. Bhat, M.F. Bekheet, A. Gurlo, Compact low
5 power infrared tube furnace for in situ X-ray powder diffraction, *The Review of scientific*
6 *instruments* 88 (2017) 13903. <https://doi.org/10.1063/1.4973561>.
- 7 [25] L. Schlicker, A. Doran, P. Schnepfmüller, A. Gili, M. Czasny, S. Penner, A. Gurlo,
8 Transmission in situ and operando high temperature X-ray powder diffraction in variable
9 gaseous environments, *The Review of scientific instruments* 89 (2018) 33904.
10 <https://doi.org/10.1063/1.5001695>.
- 11 [26] O. Karnland, S. Olsson, U. Nilsson, Mineralogy and sealing properties of various
12 bentonites and smectite-rich clay materials. (2006). Swedish Nuclear Fuel and Waste
13 Management Co, Stockholm, <http://www.skb.se/upload/publications/pdf/TR-06-30.pdf>
14 (accessed 31 August 2019).
- 15 [27] C.N. Achilles, R.T. Downs, D.W. Ming, E.B. Rampe, R.V. Morris, A.H. Treiman, S.M.
16 Morrison, D.F. Blake, D.T. Vaniman et al., Mineralogy of an active eolian sediment from the
17 Namib dune, Gale crater, Mars, *J. Geophys. Res. Planets* 122 (2017) 2344–2361.
18 <https://doi.org/10.1002/2017JE005262>.
- 19 [28] CLASS Exolith Lab, Datasheet for MGS-1 Mars Global Simulant: (March 2019). Cannon,
20 Kevin M., Conroy, Mike, Britt, Daniel T. University of Central Florida, USA,
21 https://sciences.ucf.edu/class/simulant_marsglobal (accessed 20 April 2020).
- 22 [29] C. Vogt, J. Lauterjung, R.X. Fischer, Investigation of the Clay Fraction (<2 µm) of the
23 Clay Minerals Society Reference Clays, *clays clay miner* 50 (2002) 388–400.
24 <https://doi.org/10.1346/000986002760833765>.

- 1 [30] F. Kraehenbuehl, H.F. Stoeckli, F. Brunner, G. Kahr, M. Mueller-Vonmoos, Study of the
2 water-bentonite system by vapour adsorption, immersion calorimetry and X-ray techniques:
3 I. Micropore volumes and internal surface areas, following Dubinin's theory, Clay miner. 22
4 (1987) 1–9. <https://doi.org/10.1180/claymin.1987.022.1.01>.
- 5 [31] S.L. Teich-McGoldrick, J.A. Greathouse, C.F. Jové-Colón, R.T. Cygan, Swelling
6 Properties of Montmorillonite and Beidellite Clay Minerals from Molecular Simulation:
7 Comparison of Temperature, Interlayer Cation, and Charge Location Effects, J. Phys. Chem.
8 C 119 (2015) 20880–20891. <https://doi.org/10.1021/acs.jpcc.5b03253>.
- 9 [32] J.L. Bishop, Infrared Spectroscopic Analyses on the Nature of Water in Montmorillonite,
10 clays clay miner 42 (1994) 702–716. <https://doi.org/10.1346/CCMN.1994.0420606>.
- 11 [33] O. Karnland, Chemical and mineralogical characterization of the bentonite buffer for the
12 acceptance control procedure in a KBS-3 repository. (2010). Swedish Nuclear Fuel and
13 Waste Management Co, Stockholm,
14 https://inis.iaea.org/search/search.aspx?orig_q=RN:43003619 (accessed 27 November
15 2019).
- 16 [34] M. Müller-Vonmoos, G. Kahr, Mineralogical investigations of Wyoming bentonite MX-80
17 and Montigel. (1983). ETH Zürich - Institut fuer Grundbau und Bodenmechanik,
18 [https://www.nagra.ch/data/documents/database/dokumente/\\$default/Default%20Folder/Publicationen/NTBs%201983-1984/d_ntb83-12.pdf](https://www.nagra.ch/data/documents/database/dokumente/$default/Default%20Folder/Publicationen/NTBs%201983-1984/d_ntb83-12.pdf) (accessed 20 December 2019).
- 20 [35] C. Valderrama, J. Giménez, J. de Pablo, M. Martínez, Transport of Strontium Through a
21 Ca-bentonite (Almería, Spain) and Comparison with MX-80 Na-bentonite: Experimental and
22 Modelling, Water Air Soil Pollut 218 (2011) 471–478. [https://doi.org/10.1007/s11270-010-](https://doi.org/10.1007/s11270-010-0660-1)
23 0660-1.

- 1 [36] R.F. Conley, Practical dispersion: A guide to understanding and formulating slurries,
2 VCH, New York, 1996.
- 3 [37] A. Cadene, S. Durand-Vidal, P. Turq, J. Brendle, Study of individual Na-montmorillonite
4 particles size, morphology, and apparent charge, Journal of colloid and interface science
5 285 (2005) 719–730. <https://doi.org/10.1016/j.jcis.2004.12.016>.
- 6 [38] M. Morvan, D. Espinat, J. Lambard, T. Zemb, Ultrasmall- and small-angle X-ray
7 scattering of smectite clay suspensions, Colloids and Surfaces A: Physicochemical and
8 Engineering Aspects 82 (1994) 193–203. [https://doi.org/10.1016/0927-7757\(93\)02656-Y](https://doi.org/10.1016/0927-7757(93)02656-Y).
- 9 [39] P.A. Schroeder, Clays in the critical zone, Cambridge University Press, Cambridge,
10 2018. <https://doi.org/10.1017/9781316480083>.
- 11 [40] J.R. Taylor, A.C. Bull, Ceramics glaze technology, Pergamon Press, Oxford, 1986.
- 12 [41] B. Abu-Jdayil, Rheology of sodium and calcium bentonite–water dispersions: Effect of
13 electrolytes and aging time, International Journal of Mineral Processing 98 (2011) 208–213.
14 <https://doi.org/10.1016/j.minpro.2011.01.001>.
- 15 [42] L. Bailey, H.N.W. Lekkerkerker, G.C. Maitland, Smectite clay--inorganic nanoparticle
16 mixed suspensions: Phase behaviour and rheology, Soft matter 11 (2015) 222–236.
17 <https://doi.org/10.1039/c4sm01717j>.
- 18 [43] S.W. Jeong, J. Locat, S. Leroueil, The Effects of Salinity and Shear History on the
19 Rheological Characteristics of Illite-Rich and Na-Montmorillonite-Rich Clays, clays clay
20 miner 60 (2012) 108–120. <https://doi.org/10.1346/CCMN.2012.0600202>.
- 21 [44] S.A. Wilson, D.L. Bish, Stability of Mg-sulfate minerals in the presence of smectites:
22 Possible mineralogical controls on H₂O cycling and biomarker preservation on Mars,
23 Geochimica et Cosmochimica Acta 96 (2012) 120–133.
24 <https://doi.org/10.1016/j.gca.2012.08.008>.

- 1 [45] U. Hofmann, Intracrystalline Swelling, Cation Exchange, and Anion Exchange of
2 Minerals of the Montmorillonite Group and of Kaolinite, *clays clay miner* 4 (1955) 273–287.
3 <https://doi.org/10.1346/CCMN.1955.0040132>.
- 4 [46] N. Guven, D.J. Panfil, L.L. Carney, Comparative Rheology of Water-Based Drilling
5 Fluids With Various Clays: International Meeting on Petroleum Engineering, 1-4 November,
6 Tianjin, China. 1988. Society of Petroleum Engineers, [https://www.onepetro.org/conference-](https://www.onepetro.org/conference-paper/SPE-17571-MS)
7 [paper/SPE-17571-MS](https://www.onepetro.org/conference-paper/SPE-17571-MS) (accessed 15 March 2020). <https://doi.org/10.2118/17571-MS>.
- 8 [47] L.J. Michot, E. Paineau, I. Bihannic, S. Maddi, J.F.L. Duval, C. Baravian, P. Davidson, P.
9 Levitz, Isotropic/nematic and sol/gel transitions in aqueous suspensions of size selected
10 nontronite NAu1, *Clay miner.* 48 (2013) 663–685.
11 <https://doi.org/10.1180/claymin.2013.048.5.01>.
- 12 [48] A. Kahn, Studies on the Size and Shape of Clay Particles in Aqueous Suspension¹,
13 *clays clay miner* 6 (1959) 220–236. <https://doi.org/10.1346/CCMN.1957.0060117>.
- 14 [49] G. Rytwo, A. Banin, S. Nir, Exchange Reactions in the Ca-Mg-Na-Montmorillonite
15 System, *clays clay miner* 44 (1996) 276–285. <https://doi.org/10.1346/ccmn.1996.0440212>.
- 16 [50] R.G. Holdich, I. Sinclair, Measurement of slurry solids content by electrical conductivity,
17 *Powder Technology* 72 (1992) 77–87. [https://doi.org/10.1016/s0032-5910\(92\)85024-p](https://doi.org/10.1016/s0032-5910(92)85024-p).
- 18 [51] M. Tadza, Soil-water characteristic curves and shrinkage behaviour of highly plastic
19 clays: an experimental investigation. 2011. Cardiff University, Thesis (PhD),
20 <http://orca.cf.ac.uk/55093/> (accessed 20 December 2019).
- 21 [52] C.H. Schilling, Colloid Casting, in: *Encyclopedia of Materials: Science and Technology*,
22 Elsevier, 2001, pp. 1314–1319. <https://doi.org/10.1016/B0-08-043152-6/00248-5>.
- 23 [53] A. Vertanessian, A. Allen, M.J. Mayo, Agglomerate formation during drying, *J. Mater.*
24 *Res.* 18 (2003) 495–506. <https://doi.org/10.1557/JMR.2003.0063>.

- 1 [54] A. Maskara, D.M. Smith, Agglomeration during the Drying of Fine Silica Powders, Part II:
2 The Role of Particle Solubility, *J Am Ceram Soc* 80 (1997) 1715–1722.
3 <https://doi.org/10.1111/j.1151-2916.1997.tb03044.x>.
- 4 [55] J.Y. Wong, S.L. Laurich-McIntyre, A.K. Khaund, R.C. Bradt, Strengths of Green and
5 Fired Spherical Aluminosilicate Aggregates, *J Am Ceram Soc* 70 (1987) 785–791.
6 <https://doi.org/10.1111/j.1151-2916.1987.tb04880.x>.
- 7 [56] DIN EN, Specification for masonry units – Part 4: Autoclaved aerated concrete masonry
8 units; (Reference number: EN 771-4:2011+A1:2015), 2015.
- 9 [57] G. Cesaretti, E. Dini, X. de Kestelier, V. Colla, L. Pambaguian, Building components for
10 an outpost on the Lunar soil by means of a novel 3D printing technology, *Acta Astronautica*
11 93 (2014) 430–450. <https://doi.org/10.1016/j.actaastro.2013.07.034>.
- 12 [58] D. Maskell, A. Heath, P. Walker, Use of metakaolin with stabilised extruded earth
13 masonry units, *Construction and Building Materials* 78 (2015) 172–180.
14 <https://doi.org/10.1016/j.conbuildmat.2015.01.041>.
- 15 [59] S. Sen, S. Carranza, S. Pillay, Multifunctional Martian habitat composite material
16 synthesized from in situ resources, *Advances in Space Research* 46 (2010) 582–592.
17 <https://doi.org/10.1016/j.asr.2010.04.009>.
- 18 [60] J.D. Tarnas, J.F. Mustard, H. Lin, T.A. Goudge, E.S. Amador, M.S. Bramble, C.H.
19 Kremer, X. Zhang, Y. Itoh et al., Orbital Identification of Hydrated Silica in Jezero Crater,
20 Mars, *Geophysical Research Letters* 22 (2019) 1. <https://doi.org/10.1029/2019GL085584>.